Journal of Alloys and Compounds 994 (2024) 174682

Contents lists available at ScienceDirect

Journal of Alloys and Compounds

journal homepage: www.elsevier.com/locate/jalcom

Construction of TiO_2@Cu_2O-CuS heterostructures integrating RGO for enhanced full-spectrum photocatalytic degradation of organic pollutants

Luminita Andronic [a,*], Coset Abreu-Jaureguí [b], Joaquin Silvestre-Albero [b]

[a] Product Design, Mechatronics and Environment Department, Transilvania University of Brasov, Eroilor 29, Brasov 500036, Romania
[b] Laboratorio de Materiales Avanzados, Departamento de Química Inorgánica-Instituto Universitario de Materiales, Universidad de Alicante, San Vicente del Raspeig 03690, Spain

ARTICLE INFO

Keywords:
TiO_2@Cu_2O-CuS heterostructures
Reduced graphene oxide
Full-spectrum photocatalysis
Imidacloprid degradation
Nanocomposite engineering
Environmental remediation

ABSTRACT

This study presents the development and optimization of TiO_2@Cu_2O-CuS heterostructures, enhanced with reduced graphene oxide (RGO), for efficient photocatalytic degradation of organic pollutants, focusing on imidacloprid. Two configurations, TiO_2/RGO/Cu_2O-CuS and Cu_2O-CuS/RGO/TiO_2, are explored to highlight the impact of material layering on photocatalytic efficiency. The strategic integration of RGO optimizes charge transfer, crucial for photocatalysis. Comprehensive characterization techniques, such as X-ray diffraction (XRD), Transmission Electron Microscopy (TEM), X-ray Photoelectron Spectroscopy (XPS), Raman spectroscopy, and Nitrogen adsorption-desorption isotherms, provide insights into the crystalline structure, morphology, surface chemistry, and textural properties of the heterostructures. The TiO_2/RGO/Cu_2O-CuS configuration significantly outperforms its counterpart in photocatalytic activity under full-spectrum (UV–VIS–IR) illumination, due to improved charge carrier dynamics and synergistic interactions between the composite materials. Remarkably, the TiO_2/RGO/Cu_2O-CuS assembly achieved over 95 % degradation of imidacloprid under simulated solar irradiation, marking a breakthrough in solar spectrum utilization for photocatalysis and exhibits promising recyclability, maintaining its high photocatalytic efficiency even after multiple degradation cycles, highlighting its potential for sustainable pollutant removal applications. Additionally, this configuration demonstrates a twofold increase in degradation efficiency compared to separate UV and VIS irradiations, emphasizing its rapid pollutant removal capability. This research underscores the critical role of material layer sequencing in developing high-efficiency photocatalytic systems and marks a significant advancement in environmental remediation technologies that harness renewable energy sources.

1. Introduction

Recent advancements in environmental chemistry have significantly deepened the exploration of innovative photocatalytic systems, driven by the urgent requirement to address the degradation of various pollutants [1,2]. The increasing detection of harmful organic contaminants in aquatic ecosystems [3] has spotlighted the critical need for securing uncontaminated water resources, vital for both ecological and human health [4–6]. Organic pollutants, such as pesticides, pharmaceuticals, and personal care products, have been identified as significant risks to environmental safety and public health [7–9]. Notably, the photodegradation of pesticides, especially imidacloprid, has primarily been conducted under UV and UV–VIS light, with limited exploitation under the full solar spectrum [10–13], highlighting the imperative for innovative, cost-effective pollutant removal strategies [14,15].

Globally, the increasing demand for clean water, driven by population growth, urbanization, and industrialization, underscores the importance of ensuring the availability of safe drinking water, a foundation of public health.

Photocatalysis, utilizing photocatalysts to absorb light energy for generating reactive species such as hydroxyl radicals, emerges as a promising method for eliminating organic pollutants from water [16–18]. Titanium dioxide (TiO_2) is one of the most widely used in environmental applications, especially as photocatalysts for purifying water by breaking down harmful organic pollutants [19,20]. Despite its numerous well-known benefits, TiO_2 applications in photocatalysis face significant limitations due to its poor absorption of visible light, which is the majority of solar spectrum region, and short carrier lifetime,

* Corresponding author.
E-mail address: andronic-luminita@unitbv.ro (L. Andronic).

https://doi.org/10.1016/j.jallcom.2024.174682
Received 19 January 2024; Received in revised form 11 April 2024; Accepted 28 April 2024
Available online 30 April 2024

meaning that the electrons and holes recombine rapidly, and reduce the quantum efficiency, further limiting the practical applicability of TiO_2 under ambient conditions [21]. To overcome these limitations, significant research efforts have been directed toward modifying TiO_2, either by doping with metals or non-metals, creating heterojunctions with other semiconductors [22]. These strategies aim to extend the light absorption to the visible range and improve charge carrier separation, thereby enhancing the photocatalytic activity of TiO_2 under sunlight. Notable examples include TiO_2/g-C_3N_4 [23], CdS/g-C_3N_4 [24], ZnO/g-C_3N_4 [25], WO_3/$BiVO_4$ [26], and MoS_2/WO_3 [27], which demonstrates the potential of these strategies to overcome TiO_2's limitations.

Copper-based materials, such as copper oxide [28–31] and copper sulfide [32,33], with band gaps in the range of 1.2–2.0 eV, are ideal for absorbing visible light photons [34], making them suitable for visible-light-driven photocatalysis [35,36], and are distinguished by their versatile oxidation states, enabling a wide range of photocatalytic behavior. This versatility facilitates the formation of highly effective heterostructures in photocatalysis due to their enhanced charge transfer capabilities and efficient electron-hole separation, which is crucial for the photodegradation of pollutants. The unique band alignments of CuS and Cu_2O with other metal-free nanomaterials, such as RGO, create synergistic effects that significantly improve photocatalytic efficiency.

Reduced graphene oxide (RGO) has been extensively used and investigated in composite photocatalysts due to its unique properties, which lead to an enhanced photocatalytic performance compared to graphene oxide (GO) [37]. The process of reducing GO to RGO eliminates oxygen-containing functional groups, reduces defect sites, and increases the material's electrical conductivity. This increase in electrical conductivity facilitates a better separation and transmission of photogenerated electrons and holes, the active participants in photocatalytic reaction [38]. Moreover, RGO's inclusion in composite photocatalysts not only boosts the catalysts' stability but also diminishes the recombination of photogenerated electrons and holes, thereby increasing the photocatalytic efficiency [39]. The distinctive structure and properties of RGO render it an effective electron mediator in photocatalytic systems [40], surpassing GO in several aspects: firstly, RGO's higher electrical conductivity is critical for efficient charge transfer and transport during photocatalytic reactions; secondly, low oxygen content in RGO leads to a higher surface area and more active sites for the photocatalytic reaction [41]; thirdly, RGO's lower bandgap energy makes it more suitable for visible light absorption, thus enhancing the overall efficiency of the reaction.

This study investigates the development of a unique heterostructure that integrates TiO_2, RGO, and the copper-based catalyst Cu_2O-CuS, marking a significant advancement in the field of photocatalysis. Our innovative approach lies in assembling a photocatalyst designed to utilize the entire solar spectrum, from UV to visible to infrared light, to efficiently generate reactive species capable of degrading organic pollutants. This multifaceted system harnesses the complementary strengths of its components: the broad-spectrum photocatalytic activity of TiO_2, the superior electrical conductivity and electron mediation capabilities of RGO, and the visible light absorption of Cu_2O-CuS marking a step forward in harnessing advanced photocatalytic technologies for environmental applications [42]. A novel aspect of our work is the strategic configuration of these materials into a heterostructure where TiO_2 and Cu_2O-CuS are supported on RGO sheets. This configuration optimizes the migration of photo-excited electrons from the copper-based catalyst to TiO_2 via RGO, enhancing charge separation and reducing electron-hole recombination.

Moreover, an integral aspect of our research emphasizes the stability and recyclability of the developed TiO_2/RGO/Cu_2O-CuS heterostructure, which is crucial for its practical application in environmental remediation. Our investigations reveal that this heterostructure retains its photocatalytic efficiency across multiple degradation cycles and demonstrates minimal activity loss when subjected to repeated use under solar irradiation. This resilience against photocatalytic degradation underscores the heterostructure's capability for long-term operation, a significant leap towards sustainable photocatalysis. The ease of regeneration and the consistent performance over successive cycles address two of the most pressing challenges in photocatalytic system deployment: durability and operational cost efficiency. By showcasing the heterostructure's ability to maintain high degradation efficiencies without extensive maintenance or the need for frequent catalyst renewal, our study sets a new benchmark for developing photocatalysts that are both effective and economically viable for large-scale environmental cleanup efforts.

2. Experimental section

2.1. Synthesis of base materials

2.1.1. Synthesis of graphene oxide and reduced graphene oxide

The synthesis of GO and RGO was carried out in two stages.

(i) The GO suspension was synthesized using the Hummers method [43]. Initially, 2 g of graphite, 2 g of sodium nitrate, and 96 mL of 98 % sulfuric acid were mixed in a water bath with ice for 45 minutes. Subsequently, 12 g of $KMnO_4$ was slowly added while stirring for 30 minutes in the ice bath. The mixture was then placed in a water bath set at 30°C and stirred for 90 minutes, gradually rising to 55°C. At 55°C, 80 mL of ultrapure water was added drop by drop to the mixture, and the solution was stirred for another hour to obtain a brown suspension. Then, 15 mL of 30 % H_2O_2 was added drop by drop and reacted with the excess of $KMnO_4$. The suspension was diluted to 200 mL with warm distilled water and centrifuged at 4000 rpm for 3 minutes. The supernatant was discarded, hot water was added, mixed, and sonicated, and this process was repeated three times. The final suspension was collected, measured, and diluted to 200 mL with ultrapure water, and the suspension was sonicated for 1 hour. To accurately determine the concentration of GO in the suspension, 10 mL of the suspension was placed in a weighed crucible and heated in an oven at 80°C for 16 hours. After cooling in a desiccator, the amount of GO in the suspension was calculated. This procedure was repeated three times to ensure measurement accuracy. As a result of the weight loss method, the concentration of GO in the suspension was determined to be 6 g/L.

(ii) RGO (Sample S1) was obtained by thermal reduction of the GO suspension [44]. In this process, 5 mL of GO suspension was placed in a crucible, covered with a lid, and then wrapped with aluminum foil to prevent expansion. The crucible was placed in a preheated oven at 350°C and left for 10 minutes, causing a chemical reaction to occur, resulting in the removal of oxygen-containing functional groups from the GO structure and the reduction of GO to RGO [45]. This reduction process leads to the restoration of the sp^2 hybridization of carbon atoms in the graphene lattice, forming a more ordered and conductive graphene structure [46].

2.1.2. Synthesis of TiO_2 and TiO_2/RGO

TiO_2 (Sample S3) was synthesized through a combination of sol-gel and hydrothermal processes in three steps.

(i) **Sol formation**: Initially 12.5 mL of 99.6 % ethanol was ultrasonicated for 5 minutes to ensure homogeneity. Then, 7.5 mL of titanium isopropoxide (TTIP, 99.7 % purity from Aldrich) was added dropwise for 30 minutes. A subsequent ultrasonication for an additional 30 minutes at ambient conditions ensured proper dispersion and resulted in a homogeneous solution.

(ii) **Gel formation**: 65 mL of ultrapure water was added to a Berzelius flask. Solution A (from the previous step) was then incorporated dropwise. The combination initiated a gelation process

whereby the sol transitioned to a semi-solid state, producing a TiO_2 gel.

(iii) **Hydrothermal treatment**: This gel was transferred into a sealed Teflon-lined stainless steel autoclave and heated at 150°C for 24 hours. During this phase, the titanium precursor underwent reactions in the aqueous medium to crystallize into TiO_2. Post-treatment, the formed TiO_2 crystals were isolated through filtration, followed by washing and drying, yielding a uniform, fine, white TiO_2 powder. The controlled nature of the hydrothermal process ensures a reproducible synthesis with consistent TiO_2 crystal morphology.

Synthesis of TiO_2/RGO (Sample S5): Steps 1 and 2 were as previously described in the TiO_2 synthesis. After forming the TiO_2 gel, 20 mL of GO suspension was added to the mixture to embed the GO within the TiO_2 matrix. The gel was then transferred into a sealed Teflon-lined stainless steel autoclave and heated at 150°C for 24 hours. During this phase, the titanium precursor in the gel reacted within the aqueous environment, leading to the crystallization of TiO_2. Simultaneously, the GO underwent reactions that enabled the formation of TiO_2 nanoparticles anchored onto the GO sheets. After the hydrothermal treatment, the product was filtered, washed, and dried. This results in the TiO_2/RGO composite, where the TiO_2 particles are firmly anchored onto the surface of RGO sheets.

2.1.3. Synthesis of Cu_2O-CuS and Cu_2O-CuS/RGO

1 mmol of copper nitrate trihydrate was mixed with 40 mL of ethylene glycol (EG) by ultrasonication for 10 minutes until complete dissolution to form a stable chelate compound $(Cu\ (EG)_2)^{2+}$. Then 2 mmol of sulfur was added and the mixture was agitated for 5 minutes by ultrasonication. Subsequently, the mixture was stirred on a magnetic stir plate at 500 rpm for 30 minutes, then transferred into a sealed Teflon-lined stainless steel autoclave and heated at 150°C for 24 hours (temperature was increased at 5 °C/min over 30 minutes, then maintained at 150°C for 24 hours), and allowed to cool naturally to room temperature. Next, the suspension was purified, with contaminants and residual precursors being removed by centrifugation at 4000 rotations per minute for three minutes. The supernatant was discarded, and the residual material underwent further cleansing with two washes with water and a single wash with ethanol, followed by a second round of centrifugation. The purified suspension was then filtered through cellulose acetate filters under vacuum conditions and dried using vacuum-based methods at 60°C for one hour, resulting in a finely-textured, brown powder.

The reaction begins by combining copper nitrate and ethylene glycol, leading the formation of copper ethylene glycolate and nitric acid (Eq. 1). Sulfur was then introduced to the mixture, reacting with copper ethylene glycolate to form CuS and ethylene glycol thiolate, with sulfuric acid generated as a byproduct (Eq. 2). In the final heated step, CuS nanoparticles undergo oxidation to form Cu_2O, utilizing oxygen from the surrounding air (Eq. 3). The final product, a composite of Cu_2O and CuS nanoparticles, is obtained (Eq. 4).

The chemical reaction can be represented as follows:

$$2Cu(NO_3)_2{\cdot}3H_2O + 2C_2H_6O_2 \rightarrow Cu(OC_2H_4OH)_2 + 2HNO_3 + 4H_2O \quad (1)$$

$$Cu(OC_2H_4OH)_2 + 2\ S \rightarrow CuS + C_2H_6O_2 + H_2SO_4 \quad (2)$$

$$2CuS + 3O_2 \rightarrow Cu_2O + 2SO_2 \quad (3)$$

Overall reaction:

$$2Cu(NO_3)_2{\cdot}3H_2O + 2C_2H_6O_2 + 2S + 3O_2 \rightarrow Cu_2O\text{-}CuS\ \text{mixture} + 4HNO_3 + 2H_2SO_4 \quad (4)$$

The synthesis of Cu_2O-CuS/RGO material (Sample S4) followed the same steps as the Cu_2O-CuS synthesis, with the addition of 20 mL of GO suspension before transferring the mixture into the hydrothermal system. The reduction of GO to RGO, facilitated by ethylene glycol as the reducing agent in a hydrothermal synthesis, was observed. This process resulted in a decreased oxygen content and improved electrical conductivity of the final product, thereby enhancing its optical and electronic properties. The hydrothermal process provides a convenient and efficient method for reducing graphene oxide using ethylene glycol as the reducing agent [47].

2.2. Synthesis of heterostructure photocatalysts

The fabrication of heterostructure photocatalysts, including Cu_2O-CuS/RGO/TiO_2 (Sample S6) and TiO_2/RGO/Cu_2O-CuS (Sample S7), involves a complex integration of materials, such as Cu_2O-CuS, RGO, and TiO_2. These photocatalysts are constructed with particular emphasis on creating a tandem architecture that fosters efficient electrons and holes transfer among Cu_2O-CuS, TiO_2, and RGO, improving stability, higher electrical conductivity, and superior photocatalytic activity. This makes them well-suited for degrading wastewater pollutants. The fabrication methodologies employ sol-gel and hydrothermal techniques, aiding in the formation of these heterostructured nanocomposites.

2.2.1. Synthesis of the TiO_2/RGO/Cu_2O-CuS heterostructure

The TiO_2/RGO/Cu_2O-CuS heterostructure was synthesized by integrating previously prepared base materials. The process begins with the synthesis of TiO_2, involving the sol-gel and hydrothermal methods, as detailed in Section 2.1.2. Concurrently, GO was prepared using the Hummers method (Section 2.1.1) and was converted to RGO through thermal reduction. The Cu_2O-CuS component, synthesized as described in Section 2.1.3, was then incorporated into the TiO_2/RGO mixture. This combined suspension underwent hydrothermal treatment to promote the crystallization and phase stabilization of the heterostructure. The final TiO_2/RGO/Cu_2O-CuS nanocomposite was isolated and purified through centrifugation, washing, and drying. Fig. 1 provides a schematic representation of the synthesis process for this heterostructure, illustrating the sequential integration of the various components and the methods used.

2.2.2. Synthesis of the Cu_2O-CuS/RGO/TiO_2 heterostructure

The preparation of the Cu_2O-CuS/RGO/TiO_2 heterostructure follows a similar methodology but varies in the sequence of material integration. Initially, the Cu_2O-CuS/RGO precursors were prepared by incorporating GO to ensure its even distribution within the precursor matrix. This step leverages the previously synthesized GO and RGO materials (Section 2.1.1) and the Cu_2O-CuS synthesis method (Section 2.1.3). Simultaneously, TiO_2 was synthesized as outlined in Section 2.1.2. The Cu_2O-CuS/RGO suspension was then carefully combined with the TiO_2 suspension to ensure homogeneity. The mixture underwent hydrothermal treatment at 150°C for 24 hours, facilitating the formation of a well-integrated heterostructured photocatalyst. Post-treatment, the product underwent centrifugation, washing, and drying, similar to the process described in Section 2.2.1. This results in the formation of the Cu_2O-CuS/RGO/TiO_2 heterostructure.

2.3. Characterization methods

The crystal pattern information of the samples was analyzed using a PANalytical Empyrean X-ray diffraction equipment (Malvern, USA) with a Cu Kα cathode at 40 kV and 40 mA ($\lambda = 1.54$ Å), and a PIXcel 3D detector, in the 2Theta range of 10–80°, at a scanning speed of 5°/min. X-ray photoelectron spectroscopy (XPS) measurements were carried out using a fully automated Thermo-Scientific spectrometer with a monochromatic Al Kα X-ray source ($h\nu = 1486.6$ eV) to determine the changes in surface composition, elemental analysis and oxidation state of the as-synthesized heterojunctions. Raman spectroscopy was used to examine the vibrational modes of the materials, providing information about the structural changes that may have occurred during synthesis. Raman

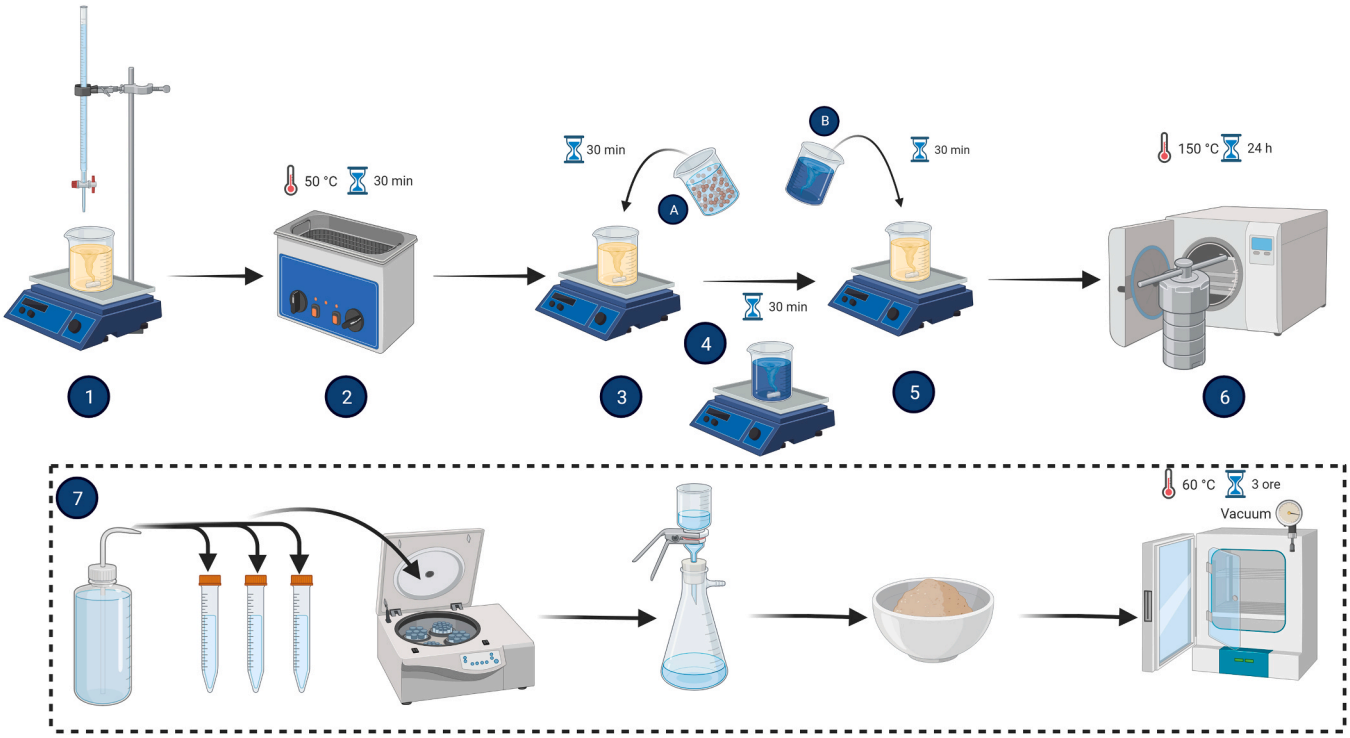

Fig. 1. Schematic description of the TiO_2/RGO/Cu_2O-CuS nanocomposite synthesis process. The steps from 1 to 7 are: 1. TiO_2 synthesis, 2. Ultrasonic processing, 3. Graphene oxide integration (A is the GO suspension), 4. Cu_2O-CuS Precursor Creation (B is a mixture of copper nitrate, ethylene glycol, and sulfur), 5. Suspension Merging, 6. Hydrothermal Synthesis, 7. Isolation & Purification.

spectra were recorded on a Raman Jasco NRS-5100 dispersive equipment using 532.11 nm as the laser excitation wavelength with a power of 2.1 mW at a resolution of 6.87 cm^{-1}/pixel. Transmission electron microscopy (TEM) was used to visualize the morphology of the nanocomposites, providing information about their particle size, shape, and distribution. TEM images were recorded using a JEOL JEM-1400 Plus apparatus equipped with an electron beam of 120 keV and an image acquisition camera model Gatan brand ORIUS.

UV-Vis-NIR spectrophotometer Jasco V-670 was used to collect UV–vis diffuse reflectance spectra (UV-DRS), in the range of 200–800 nm. The methodology to determine indirect and direct bandgaps from UV–visible diffuse Reflectance Spectroscopy (UV-Vis DRS) measurements involves the reflectance data (R) converted to the Kubelka-Munk function $F(R)$), which is related to the absorption coefficient [48]. The conversion is done using Eq. 5.

$$F(R) = \frac{(1-R)^2}{2R} \tag{5}$$

The F(R) data were plotted against the photon energy (in eV) to estimate the bandgap. The plot is for $[F(R)\cdot h\nu]^2$ for direct bandgap materials versus $h\nu$, where $h\nu$ is the photon energy. The plot is for $[F(R)\cdot h\nu]^{1/2}$ versus $h\nu$ for indirect bandgap materials. The absorption edge of the plot corresponds to the bandgap of the material.

Automatic Gas Adsorption Analyzer (AUTOSORB-iQ-XR-2, QuantaTec Inc., and Micromeritics Tristar II Plus) was used to measure the Brunauer–Emmett–Teller (BET) specific surface areas and porosity of the samples at liquid nitrogen temperature (77.3 K).

2.4. Photocatalytic experiments

Imidacloprid (IMD) was selected as the model pollutant to evaluate the photocatalytic activity of the materials prepared. IMD is indicative of various organic contaminants frequently found in water and wastewater, demonstrating unique properties and behaviors under photocatalytic conditions.

The reactor utilized for the photocatalysis comprises a stainless steel body equipped with a lid. Irradiation from a source positioned 10 cm perpendicular to the reactor's body passes through a quartz window with a diameter of 50 mm. A 160-watt bulb, capable of emitting a full spectrum of solar radiation, including UV, visible, and near-infrared light, was used for irradiation. An Avantes spectrometer (AvaSpec-ULS2048CL), used with Avasoft, facilitated measuring the entire irradiation spectrum from 200 to 1100 nm. Fig. 1S depicts the spectral irradiance as a wavelength function within the 200–1100 nm range. This bulb emits a broad range of radiation, with peaks at 313, 334, and 365 nm in the ultraviolet (UV) range, indicating strong UV emissions. Peaks at 404, 435, 546, and 577 nm fall within the visible light region, showing the bulb's significant visible light output. Lastly, the peak at 1014 nm is within the near-infrared region, highlighting the bulb's capability to emit near-infrared radiation, thus offering a comprehensive simulation of the natural sunlight spectrum. The Datalogger Einstein, equipped with sensors specialized for UVA (315–400 nm) and UVB (280–315 nm), was used to quantify the incident UVA and UVB intensities from the bulb, measuring 1250 mW/cm^2 and 415 mW/cm^2, respectively.

In this study, control experiments were conducted under similar conditions but without the presence of the photocatalyst to quantify the photolytic degradation of imidacloprid. The results from these control experiments allowed us to isolate the photolytic contribution from the overall degradation process. Thus, the data presented in our manuscript reflects the photocatalytic contribution, ensuring that the observed degradation efficiency is attributed correctly to the action of the photocatalyst.

In the experimental setup, one g/L of the photocatalyst was dispersed into 100 mL of the pollutant solution, initially at a concentration of 20 mg/L. The solution's pH was maintained unchanged. The mixture was stirred at 500 rpm in the dark for 30 minutes to allow the photocatalyst to adsorb and equilibrate with the pollutant, ensuring the

photocatalyst reached its maximum adsorption capacity and the pollutant was uniformly distributed over the photocatalyst's surface. During the photodegradation reaction, 500 μL samples were periodically extracted, filtered through a Milex 0.22 μm PES filter to remove photocatalyst particles, and then analyzed via HPLC (Shimadzu LC-20ADsp equipped with an SPD-20A UV detector set to 270 nm). The column utilized was a Macherey Nagel Nucleosil 100–5 C18, with 5 μm particle size, and maintained at 40°C. The analysis was performed with an isocratic mobile phase consisting of 20 % water and 80 % acetonitrile, an injection volume of 20 μL, and a 1.2 mL/min flow rate. The photodegradation efficiency (η) was calculated using Eq. 6, where C_0 is the initial concentration of the pollutant, and C is the concentration of the pollutant after a specific time (t).

$$\eta = \frac{C_0 - C}{C} \bullet 100 \quad (6)$$

3. Results and discussion

3.1. Photocatalysts characterization

3.1.1. Structural characterization and surface area analysis

Fig. 2 shows the XRD patterns for Cu_2O-CuS (Samples S2), TiO_2 (Samples S3), Cu_2O-CuS/RGO/TiO_2 (Sample S6), and TiO_2/RGO/Cu_2O-CuS (Sample S7). The different phases present in the samples are labeled as follows: C for cuprite (Cu_2O) with JCPDS Card No: 96–900–7498, Cu for metallic copper with JCPDS Card No: 96–710–1270, A for anatase with JCPDS Card No: 96–500–0224, B for brookite, * for CuS, and S for sulfur with JCPDS Card No: 01–072–2402.

The XRD patterns indicate the presence of the anatase phase of TiO_2 in Sample 3, as evidenced by the diffraction peaks observed at 2θ = 25.3°, 36.18°, 37.95°, 38.95°, 47.09°, 51.35°, 53.68°, 55.27°, 61.47°, 62.47°, 68.96°, and 70.19°. These peaks correspond to the (101), (103), (004), (112), (200), (202), (105), (211), (213), (204), (116), and (220) crystal planes, respectively, which are consistent with the JCPDS No. 96–500–0224. In addition, a low-intensity peak detected at 2θ = 30.2° corresponds to the (121) crystal plane of brookite, which was observed only in Sample 3. However, the anatase phase is the predominant phase in all samples where TiO_2 is present. The XRD pattern for Sample S2 reveals that the dominant phase present is cuprite (Cu_2O), denoted as C, but a certain amount of CuS is also detected. The presence of sulfur as an impurity from the synthesis process is also detected. Three clear peaks at angles 2θ = 43.4, 50.6, and 74.2°, which were identified as the Cu(111), Cu(200), and Cu(220) crystal planes of pure copper with a face-centered cubic structure (according to the JCPDS Card No. 96–710–1270).

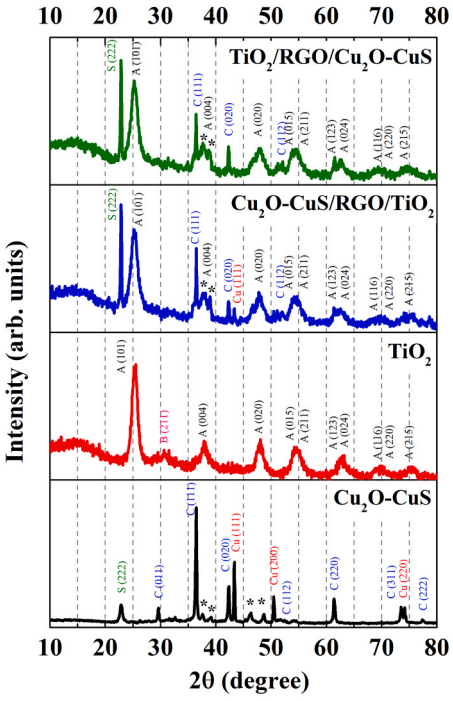

Fig. 2. XRD Patterns for Cu_2O-CuS (Samples S2), TiO_2 (Samples S3), Cu_2O-CuS/RGO/TiO_2 (Sample S6), and TiO_2/RGO/Cu_2O-CuS (Sample S7), C represents cuprite (Cu_2O) (JCPDS Card No: 96–900–7498), Cu denotes metallic copper (JCPDS Card No: 96–710–1270), A represents anatase (JCPDS Card No: 96–500–0224), B represents brookite, * represents CuS, and S represents sulfur (JCPDS Card No: 01–072–2402).

On the other hand, the XRD patterns for Samples S6 and S7 show the presence of anatase phase (A), but there is no evidence of brookite (B) in either sample. The XRD patterns of Samples S6 and S7 show an increase in the intensity of the sulfur peak (S) at 28.85 degrees (Millex index 222). Cuprite (Cu_2O) is present in both samples at 36.35 and 42.32 degrees, corresponding to crystal planes of (111) and (020), respectively. Two small peaks of CuS are also detected at 37–38 degrees in both patterns. The absence of the graphite oxide peak at 2θ = 11 degree in Samples S6 and S7 confirmed that the reduction of GO to RGO occurred during the hydrothermal synthesis of the heterostructures. While XRD analysis provides information on the crystal structure of the samples, XPS and Raman analysis can offer insights into the chemical and physical properties, such as the oxidation states and vibrational modes of the elements and compounds in the samples.

The TEM image depicted in Fig. 3a displays reduced graphene oxide (RGO) with a crumpled appearance and a disordered, three-dimensional morphology. The image shows the presence of the dark circle displays traces of sp^3-carbon. This suggests that the graphene sample is well-formed and has a high degree of crystallinity, as overlapping layers indicate a stacked arrangement of graphene sheets. The observation of graphene layers is consistent with the XRD analysis results that indicate the sample is composed primarily of graphene.

The TEM image of Sample S2 (Fig. 3b) provides a detailed morphological view of the Cu_2O-CuS composite nanoparticles. The image shows plenty of round particles with variations in size and contrast. Particles around 40 nm in diameter and smaller particles approximately 20 nm in size are also scattered throughout the micrograph. Rare specimens of much larger particles, around 120 and 160 nm, emphasize the broad size distribution. This variety in particle sizes could arise from the conditions during the synthesis process, where nucleation and growth mechanisms can be influenced by various factors such as temperature, precursor concentration, and reaction time. The darker regions within the aggregates are suggestive of the Cu_2O phase, attributed to its higher electron density compared to CuS. Conversely, the lighter particles interspersed among the darker regions likely represent the CuS phase. The proximity of the Cu_2O and CuS particles indicates a potential synergistic interaction between the two phases.

Upon examining the TEM image of the TiO_2 sample, the morphological complexities of the TiO_2 nanostructures become evident. Notably, based on the TEM analysis, the size of a single TiO_2 nucleus is approximately 8 nm. The larger, micron-sized particles apparent in the images arise due to these 8 nm nuclei aggregation. Fig. 3c, with a scale of 1 μm, showcases clusters of TiO_2 particles. The formation of these clusters can be largely attributed to the presence of amorphous TiO_2, which is likely a result of the relatively low synthesis temperature of 150°C. The growth process, underpinned by the hydrolysis–condensation reaction, gives rise to Ti-O-Ti chains. These chains act as molecular binders, fostering the interlinking of nanocrystallites [49]. The interconnected clusters suggesting a porous network, observed in Fig. 2d, indicate a high surface-to-volume ratio. This observation aligns with the measured surface area of approximately 190 m^2/g.

Fig. 3e details the nanostructures of Cu_2O-CuS/RGO (Sample S4). An amalgamation of layered sheets with numerous dispersed particles is visually present. This sheet-like morphology is characteristic of RGO, a supporting substrate for depositing Cu_2O and CuS nanoparticles. The

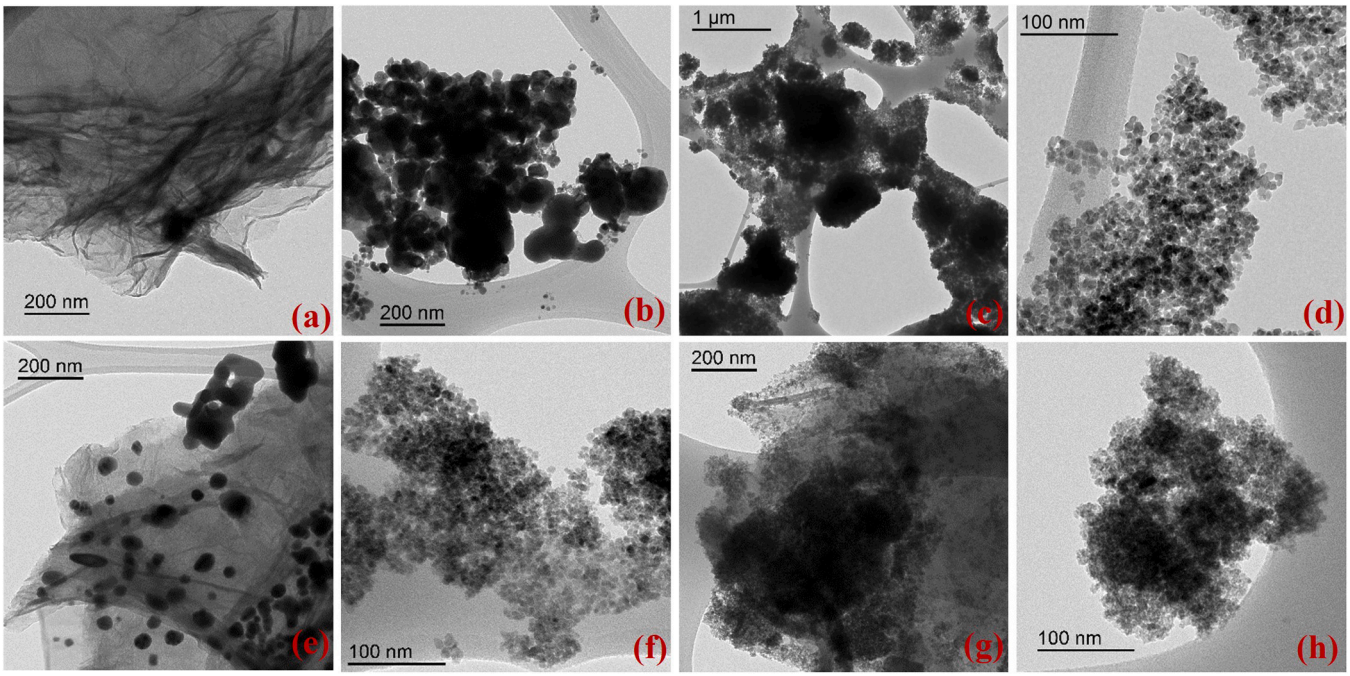

Fig. 3. TEM images of the synthesized materials: (a) RGO, (b) Cu_2O-CuS, (c,d) TiO_2, (e) Cu_2O-CuS/RGO (f) TiO_2/RGO, (g) Cu_2O-CuS/RGO/TiO_2 (h) TiO_2/RGO/Cu_2O-CuS.

dark, distinct nanoparticles sprinkled across the RGO sheet are likely the Cu_2O and CuS nanoparticles. While most particles are in the range of 20–40 nm, there are also larger particles, suggesting different stages of growth and aggregation. The close contact between the Cu_2O-CuS nanoparticles and the RGO sheets indicates strong interactions, possibly through various chemical and physical forces. Such interactions can facilitate improved electron transport between the metal oxides and RGO.

Fig. 3f presents a TEM image of the TiO_2/RGO composite (Sample S5). The visible structure comprises a juxtaposition of dense agglomerations and more transparent regions. The dense regions predominantly represent the TiO_2 nanoparticles attached to the RGO sheets. The sizes of TiO_2 are in the range of 10–30 nm, and they are uniformly distributed over the RGO layers.

Figs. 3g and 3h show a comprehensive view of the nanostructures, specifically focusing on the heterostructures of Cu_2O-CuS/RGO/TiO_2 (Sample S6) and TiO_2/RGO/Cu_2O-CuS (Sample S7), respectively. In Fig. 3g (Sample S6), the architecture starts with a Cu_2O-CuS core, intricately embedded within an RGO matrix, further enveloped by a TiO_2 shell. The darker regions depict the Cu_2O and CuS nanoparticles, indicating their higher electron densities, which appear densely packed and distributed. This core structure is surrounded by the lighter, grain-like TiO_2 nanoparticles. The presence of RGO, discernible by its characteristic sheet-like morphology, acts as a bridge connecting the inner core to the outer TiO_2 layer. On the other hand, Fig. 3h (Sample S7) presents an inversion in this architecture. Here, a TiO_2 core is encapsulated by the RGO, which subsequently is embedded with the Cu_2O-CuS nanoparticles. The TiO_2 nanoparticles manifest as finer grains interspersed within the RGO layers, while the darker regions symbolize Cu_2O-CuS. Whether TiO_2 enveloping Cu_2O-CuS or vice versa, each design offers unique possibilities for electron transfer dynamics and photocatalytic performance of heterostructures.

The textural properties of the heterostructures and their base components, including surface area, pore volume and diameter, and average particle size, were explored through N_2 adsorption-desorption analysis, with the comprehensive data summarized in Table 1. The N_2 adsorption-desorption isotherms and the derived DFT pore size distributions are displayed in Fig. 4.

Table 1
Textural properties from N_2 adsorption-desorption analysis of heterostructures and their constituent materials.

Sample	Material	Surface Area[a] (m^2 g^{-1})	S_C[b] (m^2 g^{-1})	Total micropore volume[c] (cm^3 g^{-1})	Total pore volume[d] (cm^3 g^{-1})	Average pore diameter[e] (nm)	Average particle size[f] (nm)
S2	Cu_2O-CuS	20	28	$6.5{\cdot}10^{-4}$	0.119	16.76	306
S3	TiO_2	191	220	$3.5{\cdot}10^{-4}$	0.268	4.86	31.4
S4	Cu_2O-CuS/RGO	11	15	$4.1{\cdot}10^{-4}$	0.01	4.69	541
S5	TiO_2/RGO	230	245	$13.7{\cdot}10^{-4}$	0.181	2.96	26
S6	Cu_2O-CuS/RGO/TiO_2	196	200	$48.5{\cdot}10^{-4}$	0.170	3.4	30.5
S7	TiO_2/RGO/Cu_2O-CuS	199	229	$44.9{\cdot}10^{-4}$	0.195	3.4	30.2

[a] Specific surface area data was calculated using the multi-point BET method.
[b] Barrett, Joyner, and Halenda (BJH) desorption cumulative surface area (S_C) represents the cumulative surface area of pores with diameters ranging from 1.7 nm to 300 nm.
[c] This value indicates the volume of pores that typically have diameters less than 2 nm and is calculated using the t-plot method.
[d] BJH desorption total pore volume refers to the total volume of pores within the specified range of diameters (1.7 nm to 300 nm).
[e] BJH desorption average pore diameter.
[f] calculated from the BJH equation from the analysis of the desorption curve.

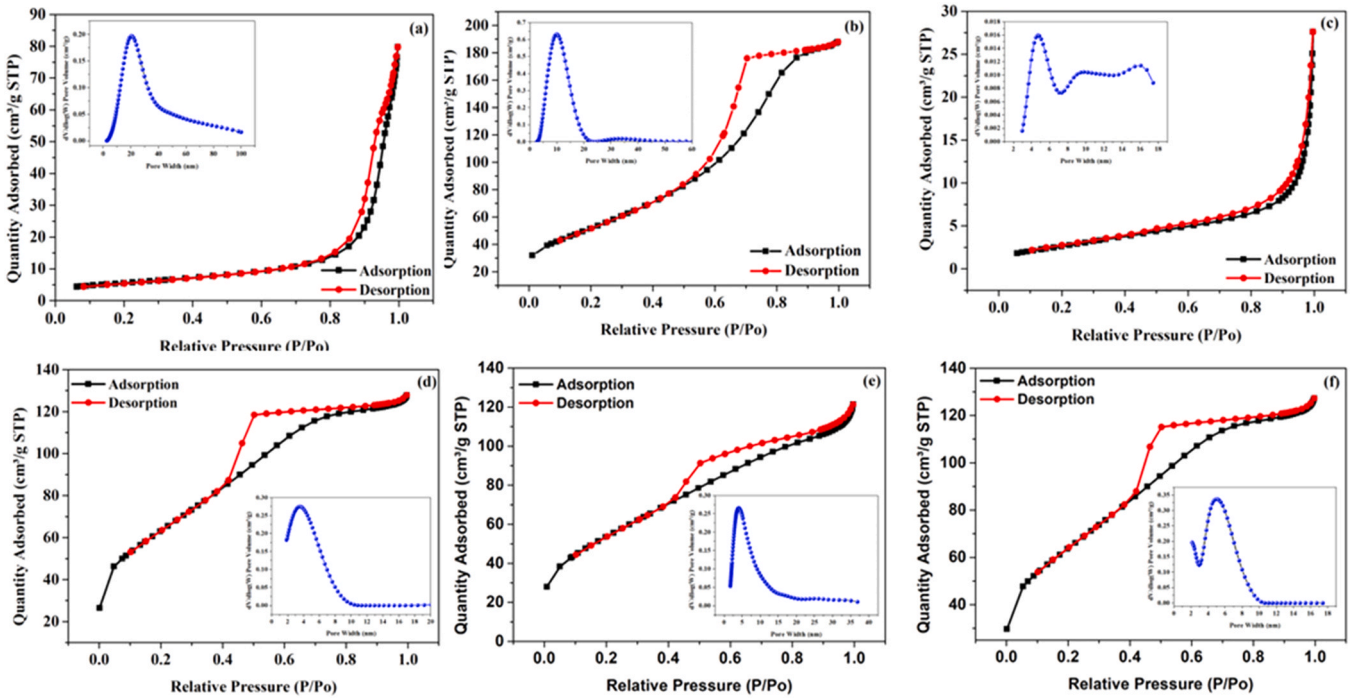

Fig. 4. N_2 adsorption-desorption isotherms and DFT-derivative pore size distribution (insets) of (a) Cu_2O-CuS, (b) TiO_2, (c) Cu_2O-CuS/RGO, (d) TiO_2/RGO, (e) Cu_2O-CuS/RGO/TiO_2, (f) TiO_2/RGO/Cu_2O-CuS.

The isotherms of Cu_2O-CuS (Fig. 4a) and Cu_2O-CuS/RGO (Fig. 4c) show the presence of some microporous together with a small hysteresis loop at high pressures, pointing to nitrogen condensation in the inter-particle space and/or in large mesopores. The pore size distributions suggest a shift from predominantly 20–30 nm mesopores in Cu_2O-CuS to narrower 4–8 nm mesopores in Cu_2O-CuS/RGO, corresponding with a lower surface area of 20 m^2/g and 11 m^2/g, respectively. This reduced surface area may result from the compact arrangement of the narrower mesopores, thereby decreasing the total surface available for gas adsorption.

The isotherms for TiO_2 (Fig. 4b) and TiO_2/RGO (Fig. 4d) resemble type-IV with H3 hysteresis loops, indicative of mesoporous textures [50]. The observed hysteresis loops spanning from a P/P_o value of 0.4–0.9 in TiO_2 and the peak pore sizes ranging from 10 to 20 nm in TiO_2 to 2–8 nm in TiO_2/RGO demonstrate variations in porosity due to RGO integration. This is also reflected in the higher specific surface area of the TiO_2/RGO composite (230 m^2/g) compared to pure TiO_2 (191 m^2/g), highlighting RGO's role in enhancing the textural properties.

Comparatively, the heterostructures of Cu_2O-CuS/RGO/TiO_2 and TiO_2/RGO/Cu_2O-CuS, examined in Figs. 4e and 4f, showcase isotherms with Type IV characteristics and H3 hysteresis, suggestive of capillary condensation in mesopores and a pore width range from 2 to 10 nm [51]. These features are conducive to photocatalytic activity due to improved mass transport and accessible catalytic sites.

Compared to their individual components, both heterostructures Cu_2O-CuS/RGO/TiO_2 and TiO_2/RGO/Cu_2O-CuS demonstrate a superior specific surface area, essential for providing abundant active sites for photocatalysis, with a surface area of 196 m^2/g, and respectively 199 m^2/g, outperform Cu_2O-CuS and Cu_2O-CuS/RGO, which have surface areas of 20 m^2/g and 11 m^2/g, respectively. This increase in surface area is accompanied by a higher total micropore volume in both heterostructures, suggesting a more intricate porosity that can facilitate molecule-catalyst interactions, a desirable for photocatalytic reactions. In contrast, the individual constituents, such as TiO_2 with a lower micropore volume of $3.5{\cdot}10^{-4}$ cm^3/g and TiO_2/RGO with $13.7{\cdot}10^{-4}$ cm^3/g, illustrate the additional microporous nature introduced in the composites.

The heterostructures maintain average pore diameters similar to those of the individual components, indicating a consistent pore size distribution crucial for reactant access and diffusion. The particle size of heterostructures is intermediate compared to their constituents, suggesting a balanced agglomeration that promotes light absorption and maintains reactant dispersion.

When correlating these textural properties with the photocatalytic activities discussed in Section 3.2, the role of the structural attributes becomes evident. The TiO_2/RGO/Cu_2O-CuS heterostructure exhibits the highest rate constant values, which points to an optimized electron-hole separation and effective charge transfer pathways. This optimized heterostructure, therefore, enables them to utilize the full-spectrum radiation more efficiently, leading to their superior photocatalytic performance compared to the individual components. The heterostructures, through a beneficial combination of surface area, pore volume, and particle size, harness the advantages of each constituent material, thus providing improved photocatalytic properties. Integrating individual photocatalytic materials can synergistically enhance photocatalytic performance, as demonstrated by the rate constants in the presence of full-spectrum radiation.

3.1.2. *Surface chemistry and oxidation states revealed through XPS*

The photocatalytic efficiency of nanocomposites depends on their intrinsic properties, such as chemical states and bonding structures. X-ray photoelectron spectroscopy (XPS), known for its surface sensitivity, was deployed to solve these elements.

XPS analysis shows significant peaks corresponding to the nanocomposite's elemental composition: C 1 s at 284–291 eV, O 1 s at 529–535 eV, Cu 2p at 930–960 eV, Ti 2p at 455–468 eV, and S 2p, at 160–169 eV. These results align with Raguram et al. [52] and Huang et al. [53], who reported similar peak positions for these elements. Detailed peak analysis provided insights into the chemical oxidation states of copper (Cu), titanium (Ti), and sulfur (S), as well as the oxygen functionalities' interaction with RGO [54].

3.1.2.1. Reduced graphene oxide (RGO). For RGO (Sample S1), the XPS

spectrum, depicted in Fig. 2S(a), confirmed the presence of distinct carbon-related functional groups. The peak at 284.58 eV indicated the presence of C═C bonds, while the peak at 286 eV was associated with C-OH functional groups. The peak revealed the presence of C═O functional groups at 287 eV, and the peak at 288.5 eV suggested the presence of carboxylic acid groups, represented by HO-C═O. The XPS analysis determined the degree of oxidation and the functional groups present, consistent with previous studies by Liu [37]. The C 1 s peak observed in the XPS spectra of RGO is typically found between 284 and 286 eV, which is consistent with the presence of sp^2 hybridized carbon atoms in the graphene layers. Furthermore, the C 1 s peak can be split into multiple components corresponding to different carbon species, such as carbon atoms in oxygen-containing functional groups or sp^2 hybridized carbon atoms in the graphene layers. The O 1 s peak is typically found between 532 and 534 eV, which can be used to determine the oxygen content and the presence of any oxygen-containing functional groups. The XPS analysis of RGO provides valuable information regarding the carbon and oxygen content and the functional groups present on the material's surface.

3.1.2.2. Titanium dioxide (TiO_2). The Fig. 2S(b) XPS spectrum of TiO_2 (Sample S3) shows a peak around 458 eV in the Ti 2p region, suggesting that the titanium is fully oxidized as Ti^{4+}. This observation aligns with a high-quality, pristine titanium dioxide sample.

3.1.2.3. Titanium dioxide-reduced graphene oxide (TiO_2-RGO). The XPS spectrum of the TiO_2-RGO sample (Sample S5) (Fig. 2S(c)) showed that the two peaks corresponding to Ti $2p^{1/2}$ and Ti $2p^{3/2}$ were unmodified compering with TiO_2 (Fig. 2S(d)), suggesting that there was no carbon doping in the TiO_2 network or Ti^{3+} suggests that the sample is free from titanium in a reduced state or from any significant defect levels associated with Ti^{3+}. The XPS spectrum of the TiO_2-RGO sample showed that the energetic peaks of the C═C and C-OH bonds were unmodified compared to RGO. However, modifications were observed in the C═O and HO-C═O functional groups, identified at 286.68 eV and 289.28 eV, respectively. The spectrum further indicates shifts in specific carbon-related functional groups due to the likely chemical interaction between TiO_2 and RGO.

3.1.2.4. Copper oxide-sulfide (Cu_2O-CuS). Fig. 3S(a-c) displays the XPS spectra, revealing the surface atomic composition and chemical state of the Cu_2O-CuS sample (Sample 2). The spectra clearly show the presence of Cu, S, and O elements, reflecting the compositional characteristics of the sample. The binding energies of the Cu 2p3/2 peak at 932.28 eV and the Cu 2p1/2 peak at 951.98 eV indicate that the sample contains copper in two distinct oxidation states: Cu^+ and Cu^{2+}. Notably, the binding energy of the Cu 2p3/2 peak aligns with the reported values for Cu^+ in copper sulfides, typically around 932–933 eV. In Fig. 3S(b), the binding energies of the S 2p3/2 peak at 161.48 eV and the S 2p1/2 peak at 162.43 eV are indicative of the presence of S^{2-} ions coordinated with Cu^{2+} ions within CuS nanocrystals. Deconvolution of this spectrum reveals distinctive peaks corresponding to CuS, such as those for S^{2-} at 161.48 and 162.68 eV and S_2^{2-} at 162.38 eV. Fig. 3S(c) showcases the O 1 s XPS spectrum, which can be deconvoluted into two distinct peaks. The peak at 530.28 eV is representative of oxygen within the Cu_2O lattice structure. The concurrent presence of both Cu(I) and Cu(II) species in the Cu 2p spectrum, as well as the S^{2-} ions in the S 2p spectrum, corroborates the presence of Cu_2O and CuS phases in the sample, respectively.

3.1.2.5. Heterostructured photocatalysts. Sample S6 is characterized by a layered structure, starting with Cu_2O-CuS as the based layer, then RGO, and TiO_2 on the top. However, CuS was not detected in the S 2p region on the surface of Sample S6 (as shown in Fig. 5e), suggesting its presence within the bulk and indicating TiO_2 as the predominant surface photocatalyst.

The TiO_2/RGO/Cu_2O-CuS heterostructure differs from Sample S6, with TiO_2 as the base layer, followed by RGO and Cu_2O-CuS on top. The layer formation involved:

(1) The deposition of RGO onto TiO_2 resulted in a composite with enhanced electronic and mechanical properties. The TiO_2 XPS data showed a Ti 2p3 binding energy of 458.82 eV, typical for the Ti^{4+} oxidation state, and O 1 s binding energies ranging from

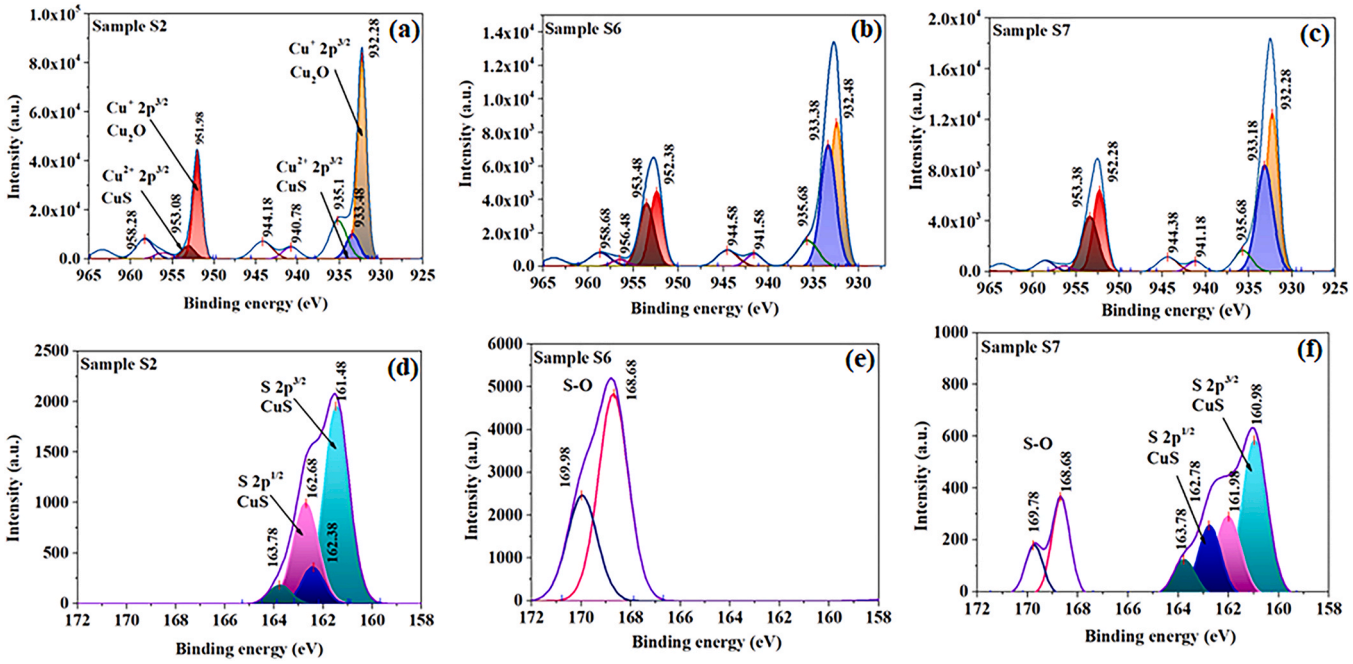

Fig. 5. XPS Spectra analysis of hybrid photocatalysts Samples S6 and S7 compared with sample S2: (a-c): Cu 2p spectrum showing the surface atomic composition and oxidation states of copper for Samples S2, S6, and S7, respectively. (d-f): S 2p spectrum displaying sulfur's coordination and its presence in CuS nanocrystals for Samples S2, S6, and S7, respectively.

530.08 eV to 533.07 eV, indicative of Ti-O bonds. The RGO layer exhibited C 1 s binding energies from 284.56 eV to 288.93 eV, consistent with sp^2 hybridized carbon structures.

(2) The subsequent layering of Cu_2O-CuS on TiO_2/RGO involved the application of a copper precursor solution, followed by sonication to achieve uniform distribution. The XPS analysis verified the presence of both Cu_2O and CuS by identifying the relevant binding energies: for S 2p3, values ranged between 160.96 eV and 162.76 eV, with a peak at 168.68 eV, characteristic of the S^{2-} oxidation state in Cu-S bonds. The Cu 2p3 binding energies for CuS and Cu_2O were noted between 932.3 eV to 935.68 eV, and 941.18 eV to 944.4 eV, respectively, suggesting the coexistence of Cu^{+} and Cu^{2+} oxidation states. The O 1 s binding energy for Cu_2O was recorded consistently between 530.08 eV and 533.07 eV, affirming the Cu-O bond.

The distinct assembly of the TiO_2/RGO/Cu_2O-CuS composite facilitates the synergistic interaction between its components, potentially enhancing the photocatalytic performance of the heterostructure. This structural arrangement can be observed in the XPS spectral data, which provides a deeper understanding of the electronic and chemical environment at the surface of these complex materials.

3.1.3. Vibrational properties and structural analysis via Raman spectroscopy

Raman spectroscopy was performed to elucidate the vibrational properties of the GO and RGO samples, providing essential insights into their structural and chemical nature [55]. Characteristic peaks, such as the D and G bands, associated with defects/disorders and the in-plane vibration of sp^2-bonded carbon atoms were observed [55]. Further details regarding peak positions, interpretations, and associated literature references can be found in the Supplementary Materials. It's worth noting that the intensity ratio (I_D/I_G) between these bands is a significant parameter in evaluating the quality and structure of graphene and its derivatives [56]. The I_D/I_G value revealed structural changes post-thermal treatment for our samples, hinting at the removal of oxygen functional groups and restoration of sp^2 hybridization.

Through Raman spectroscopy, we identified specific phonon modes indicative of the anatase phase of TiO_2. Notably, the prominent peak positions and their associated modes align with previously characterized vibrational features of anatase. For a comprehensive description of the exact peak positions, their correlation with established phonon modes, and related literature references, complete information about pristine TiO_2 is referred to in the Supplementary Materials.

Fig. 6 depicts the Raman spectra of the composite Samples S5, S6, and S7, the characteristic D and G bands associated with graphene structures are consistently observed. These bands typically appear in the ranges of 1350–1370 cm^{-1} (D band) and 1580–1600 cm^{-1} (G band) and provide valuable insights into the structural attributes and interactions in the materials. The shifts observed in these bands for Samples S5, S6, and S7, when compared with pristine graphene sheets and RGO, give insights into how the addition and arrangement of different components (like TiO_2 and Cu_2O-CuS) impact the overall structure and properties of the composite.

Pure graphene sheets typically present a well-defined D band centered around 1350 cm^{-1}, primarily occurring from defects or disorders. The G band, contrarily, derives from the in-plane vibration of sp^2-bonded carbon atoms and is usually seen around 1600 cm^{-1} [55]. Upon transitioning to RGO, slight spectral shifts become evident – specifically, the D and G bands localize at 1347 cm^{-1} and 1590 cm^{-1}, respectively. These shifts are predominantly the aftereffects of reduction processes, suggesting the retrieval of sp^2 hybridization and diminished oxygen functionalities.

The shift of the D band to 1340 cm^{-1}, juxtaposed with a slight upward transition of the G band to 1592 cm^{-1}, in the TiO_2/RGO indicates potential molecular interactions between TiO_2 nanoparticles and RGO,

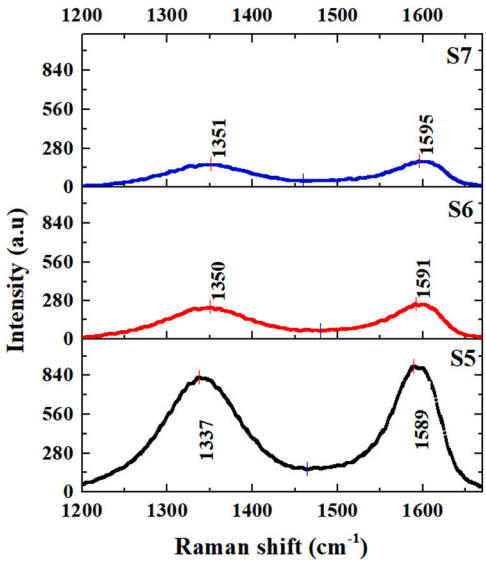

Fig. 6. D and G band intensity variations in Raman spectra of TiO_2/RGO (Sample S5), Cu_2O-CuS/RGO/TiO_2 (Sample S6), and TiO_2/RGO/Cu_2O-CuS (Sample S7).

and variations in the electronic structure, mainly from the integration of TiO_2 nanoparticles.

The complexity of Samples S6 and S7 shows more pronounced spectral transitions. Sample S6's D and G bands manifest at 1348 cm^{-1} and 1595 cm^{-1}, while for Sample S7, they are evident at 1352 cm^{-1} and 1599 cm^{-1}, respectively. Such deviations from the RGO spectra signify the potential multifaceted interactions occurring due to the incorporation of both TiO_2 and Cu_2O-CuS nanoparticles in layered structures that alter graphene's intrinsic structural and electronic properties.

3.1.4. Band gap determination using UV-Vis diffuse reflectance spectroscopy

The band gaps were evaluated using UV-Vis Diffuse Reflectance Spectroscopy (DRS) to ascertain the synthesized photocatalysts' electronic structure and optical properties. Table 2 lists materials' indirect and direct bandgap energies, some of which are intercalated with RGO. These bandgap energies are critical in determining the photocatalytic efficiency under full-spectrum irradiation, as they define the energetic threshold for electron excitation from the valence band to the conduction band.

Sample S3, consisting of pure TiO_2, exhibits indirect and direct bandgaps of 3.12 eV and 3.4 eV, respectively, that suit only ultraviolet (UV) light absorption from the full spectrum. In contrast, Sample S5, where TiO_2 is combined with RGO, shows a direct bandgap of 3.52 eV, suggesting a slight increase that could be attributed to the influence of RGO's electronic properties, possibly narrowing the bandgap to absorb less visible light. Comparatively, Sample S2, comprising Cu_2O-CuS, has an indirect bandgap of 2.09 eV and a direct bandgap of 2.45 eV, indicating a broader absorption in the visible spectrum. Incorporating RGO to form Sample S4 (Cu_2O-CuS/RGO) decreases the indirect bandgap

Table 2
Comparison of indirect and direct bandgap energies of various photocatalyst samples with and without RGO intercalation.

Sample	Materials	Indirect bandgap (eV)	Direct bandgap (eV)
S2	Cu_2O-CuS	2.09	2.45
S3	TiO_2	3.12	3.4
S4	Cu_2O-CuS/RGO	1.2	-
S5	TiO_2/RGO	-	3.52
S6	Cu_2O-CuS/RGO/TiO_2	1.7	-
S7	TiO_2/RGO/Cu_2O-CuS	1.65	-

significantly to 1.2 eV. This substantial narrowing of the bandgap with RGO intercalation points to an enhanced interaction between the Cu_2O-CuS lattice and RGO, which may introduce mid-gap states facilitating lower-energy photon absorption, thereby improving visible-light-driven photocatalytic efficiency.

For the heterostructure photocatalysts, Sample S7 (TiO_2/RGO/Cu_2O-CuS) presents an indirect bandgap of 1.65 eV, suggesting a highly efficient charge separation and transfer, which is consistent with the highest photocatalytic activity observed in Fig. 7 for this sample. The heterostructure mechanism effectively utilizes the redox potential of both semiconductor components, with RGO acting as a charge transfer mediator, enhancing the overall photocatalytic degradation of pollutants under solar irradiation. The intercalation of RGO decreases the band structure and improves charge carrier mobility and lifetime, thus facilitating higher photocatalytic efficiencies.

3.2. Photocatalytic activity of the heterostructures

Imidacloprid, a neonicotinoid insecticide, is often used as a model organic pollutant in photocatalysis studies. Due to its ability to absorb UV light, undergo photolysis, and maintain notable stability in water within a pH range of 5–9 (typical for wastewater), it stands out as an ideal candidate for examining the photocatalytic activity of photocatalytic materials. Evaluations under a full solar spectrum (including UV, visible, and infrared light) are essential for practical application. Previous our studies have demonstrated an enhanced organic pollutant photodegradation efficiency when CuS was combined with H_2O_2 [57, 58]. Nonetheless, a semiconductor with a wide band gap is essential for optimal outcomes to modulate CuS electronic structure. Therefore, Cu_2O, with a band gap close to 2.0 eV, was selected. The full-spectrum irradiation evaluations revealed that both Cu_2O-CuS and Cu_2O-CuS/RGO samples achieved a photodegradation efficiency of only 25 % after 6 hours (Fig. 7a). However, the TiO_2/RGO/Cu_2O-CuS assembly manifested a remarkable efficiency of 50 %, can be attributed to the improved charge separation and transfer capabilities inherent in the heterojunction photocatalyst. In this design, Cu_2O-CuS composite predominantly acts as visible light absorbers and electron donors, whereas TiO_2 and RGO perform roles as electron acceptors and conductors. The interaction between these components enhances the overall photocatalytic activity, increasing the degradation efficiency of imidacloprid, as depicted in Fig. 6.

Cu_2O and CuS, being p-type semiconductors, exhibit bandgap energies of 2–2.2 eV and 1.2–2.5 eV, respectively. Their inherent ability to absorb visible light, coupled with copper vacancies that operate as acceptor dopants, engenders oxidation reactions facilitated by the generated holes in the valence band. Such characteristics make these materials especially adept for photocatalytic applications under visible light. Consequently, heterostructures emerge where UV radiation primarily activates TiO_2, while visible light interacts directly with Cu_2O-CuS.

In the TiO_2/RGO/Cu_2O-CuS structure, Cu_2O-CuS crystals are situated a top the TiO_2/RGO heterostructure. In contrast, for the Cu_2O-CuS/RGO/TiO_2 configuration, TiO_2 crystals overlay the Cu_2O-CuS/RGO/ composition. This unique heterostructured layering in the TiO_2/RGO/Cu_2O-CuS photocatalyst optimizes charge separation and transfer. Upon visible light absorption by the Cu_2O-CuS component, an electron-hole pair is generated. The RGO layer then facilitates an electron transfer to the TiO_2 layer. Due to its expansive band gap, this layer captures the electrons, reducing the chances of electron-hole recombination.

For the Cu_2O-CuS/RGO/TiO_2 assembly, where the Cu_2O-CuS layer is enveloped initially by RGO and subsequently by TiO_2, the absorption of visible light appears to be subdued. This results in a diminished imidacloprid degradation efficiency. Furthermore, the isolated placement of the Cu_2O-CuS layer can amplify its susceptibility to the effects of light absorption, which could subsequently influence imidacloprid adsorption and degradation efficiency.

Fig. 8a compares the rate constants (k) for different material configurations after 6 and 24 hours of irradiation. These k values serve as indicators of photocatalytic efficiencies, and their variation clears light on the intricacies of each material's performance. The TiO_2/RGO/Cu_2O-CuS configuration exhibits the highest rate constant, with values of 0.0851 and 0.078 h^{-1} after 6 and 24 hours, respectively, suggesting an optimized charge separation and transfer, making the materials tested the most efficient. Pure TiO_2 follows closely with rate constants of 0.0735 and 0.0722 after 6 and 24 hours, respectively. Its competitive performance underlines the inherent photocatalytic strength of TiO_2, even in the absence of composite materials. The TiO_2-RGO composite yields a k value of 0.0558 h^{-1} after 6 hours, a slight reduction to 0.0468 h^{-1} after 24 hours. This indicates that while RGO might enhance certain properties, its combination with TiO_2 doesn't necessarily maximize the rate of photocatalysis. There's a discernible difference between Cu_2O-CuS/RGO/TiO_2 and Cu_2O-CuS/RGO. With rate constants of 0.0542 h^{-1} and 0.0274 h^{-1} after 6 hours, respectively, it's evident that the layering sequence plays a pivotal role in influencing the overall photocatalytic efficiency. One observation is that most materials' have relatively consistent k values from 6 to 24 hours. This suggests a stability in their photocatalytic activities over the timeframe studied.

This study evaluates the reaction rate constant (k) and degradation efficiency as key parameters for assessing the stability and recyclability of the best-heterostructured photocatalyst, TiO_2/RGO/Cu_2O-CuS. Fig. 8b presents the kinetics rate and degradation efficiency over five cycles, each lasting 24 hours. For each cycle, the initial concentration of IMD was adjusted to 20 ppm, ensuring consistency across all tests. All other conditions remain unchanged across the cycles. In Cycle 1, the rate constant was 0.078 h^{-1}, with a high degradation efficiency of 87 %. As we progress to Cycle 2, there's a slight decrease in the rate constant to

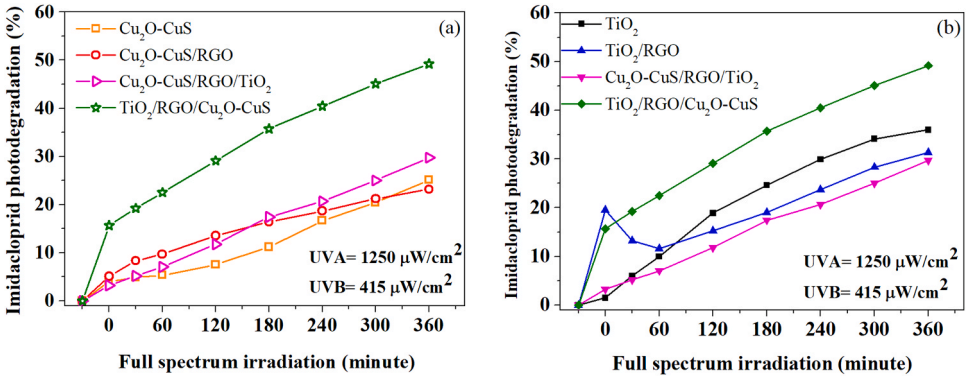

Fig. 7. Imidacloprid degradation efficiency under full-spectrum solar irradiation (290–740 nm) including UVA=1250 μW/cm^2 and UVB=415 μW/cm^2 for (a) copper-based materials and (b) TiO_2-based materials.

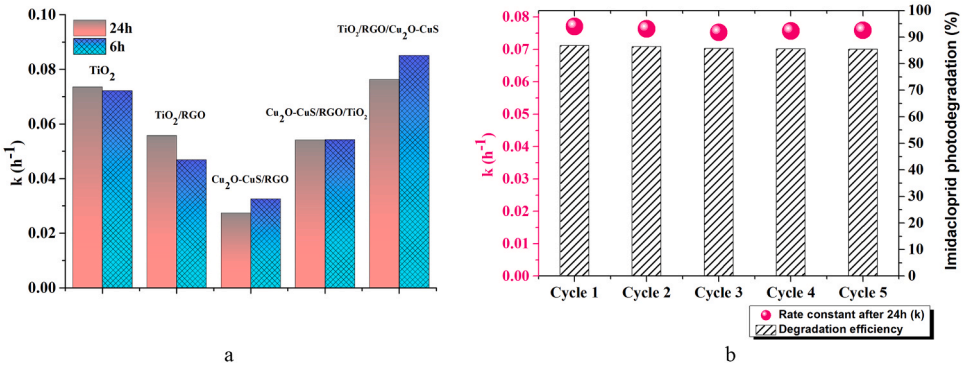

Fig. 8. a. Comparison of IMD degradation rates for various photocatalytic materials under full-spectrum solar irradiation at 6 and 24 hours, b. Stability and recyclability of heterostructure TiO_2/RGO/Cu_2O-CuS after 5 cycles.

0.07633 h^{-1} and a minimum reduction in efficiency to 86.4 %. This trend continues with further reductions in both the rate constant and efficiency in the subsequent cycles, with Cycle 3 displaying a rate constant of 0.07526 h^{-1} and efficiency of 85.7 %, and Cycle 4 showing a rate constant of 0.0757 h^{-1} with an efficiency of 85.56 %. Cycle 5 presents a minor increase in the rate constant to 0.07588 h^{-1} compared to Cycle 4, while the degradation efficiency reduces marginally to 85.43 %. This suggests that although the kinetics of the reaction remain relatively stable, the photocatalyst's effectiveness in degrading IMD diminishes slightly with each cycle. The reduction in efficiency may be attributed to the photocatalyst's active sites being partially blocked by by-products or to the minor degradation of the photocatalyst itself over repeated use. The heterostructure exhibits good stability over multiple cycles without further treatments, as indicated by the small changes in the rate constant. The recyclability has also been promising, with a minimum decrease in efficiency after five cycles for long-term applications in pollutant degradation over 24 h. The regeneration methods do not have an environmental impact, and the results are encouraging for the practical utility of heterostructure under solar irradiation.

Table 3 provides a comparative analysis of the photocatalytic performance of TiO_2@Cu_2O-CuS/RGO heterostructures against various other photocatalysts, as reported in the literature. This comparison is based on several parameters, including catalyst loading, the type and initial concentration of the pollutant treated, irradiation conditions (type, intensity, and duration), and the observed degradation rates or rate constants (k). Comparing our results with other studies, we observe a wide variation in photocatalytic efficiencies, which can be attributed to differences in catalyst composition, pollutant type, irradiation conditions, and experimental setups. Notably, our system outperforms the TiO_2@Cu_2O-CuS/RGO configuration and exhibits similar efficiency under similar conditions, highlighting the significance of the proper design of a heterostructure. The heterostructure's efficiency in utilizing the full spectrum of light, from UV to IR, is a critical factor distinguishing our system from others. This broad-spectrum utilization capability contributes to a superior photocatalytic activity observed.

3.3. *Mechanistic insights into full-spectrum photocatalytic degradation*

The diagram of the charge transfer mechanism for the TiO_2@Cu_2O-CuS heterostructure, mediated by RGO, in the photocatalytic degradation of IMD under full-spectrum irradiation is depicted in Fig. 9. The alignment of the valence and conduction bands is calculated using the methodologies described by Andronic et al. [58], employing empirical equations to determine the valence band (VB) edge potential (E_{VB}, Eq. 7) and the conduction band (CB) edge potential (E_{CB}, Eq. 8) of the semiconductors. E_{VB} (Eq. 7) is calculated based on the experimental

Table 3
Comparison of photocatalytic performance of TiO_2@Cu_2O-CuS/RGO heterostructures with literature.

Photocatalyst/catalyst loading	Pollutant type/ Initial concentration/volume	Irradiation conditions (type, intensity, and duration)	Degradation (%)/rate constants (k)	Ref.
TiO_2/RGO/Cu_2O-CuS 1 g/L Cu_2O-CuS/RGO/TiO_2 1 g/L	IMD 20 mg/L, V=100 mL	Full-spectrum fluorescent bulb solar (160 W, 30000 K), I_{UVB} = 0.228 mW/cm^2, I_{UVA} = 1.29 mW/cm^2, I_{Vis} = 137 mW/cm^2, I_{IR}=0.4 mW/cm^2	87 %, k=0.0014 min^{-1} 70 %, k=0.0009 min^{-1}	This study
Cu@TiO_2	IMD 25 mg/L, V=30 mL continuous flow reactor	Full-spectrum fluorescent bulb (15 W, 6500 K). I_{UVB} = 1.35 mW/cm^2, I_{UVA} = 2.45 mW/cm^2, I_{Vis} = 2.52 mW/cm^2,	k=0.00228 min^{-1}	[59]
Au–SnO_2–CdS 3 g/L	IMD 0.5 mg/L, V=50 mL	30 W white LED bulb, 470 nm, 19,100 lux, t=3 h	95 %, k= 0.0156 min^{-1}	[60]
ZIF-CdS/Tpy 0.7 g/L	IMD 10 mg/L, V=10 mL	simulated visible light irradiation, 35 W LED lamp, t=1.5 h	91 %, pH=7	[61]
Cu_2O@TiO_2 1 g/L	PVA 20 mg/L, V=200 mL	300 W Xenon lamp, 1000 lm/m^2	k=0.00617 min^{-1}	[62]
CuO@TiO_2 0.5 g/L	MB 3.2 mg/L	visible light source (LED bulb, λ > 400 nm), 46 W/cm^2, t=60 min	26 %, k= 0.301 h^{-1}	[63]
Cu_2O/Cu/TiO_2 1 g/L	RB 4.8 mg/L, V=50 mL	UV–VIS irradiation/Xe lamp, 150 W, 200–1000 nm, t=120 min	90 %	[36]
Cu_2O/graphene/ TiO_2 0.5 g/L	MB 5 mg/L	500 W Xenon lamp, λ > 420 nm, I_{Vis} =42.0 mW·cm^{-2}, t=100 min	39 %	[64]
Cu_2O/TiO_2/celulose nanofibre/rGO 3D monolite	MO 20 mg/L, V=50 mL	200 W Xe lamp, t=120 min	78.6 %, k= 0.01598 min^{-1}	[62]
ZnS/CuS-rGO 0.1 g/L	MB 50 mg/L, RB 50 mg/L, V=100 mL, 2 mL H_2O_2 30 %	300 W Xe lamp, simulating sunlight, lamp current 15 A, t=30 min	MB: 99.24 %, k=0.15464 min^{-1} RB: 99.19 %, k=0.15945 min^{-1}	[65]
Cu_2O–TiO_2-g-C_3N_4 0.2 g/L	MO 20 mg/L, TC 30 mg/L, V=50 mL	PCX50C Discov photoreactor, LED light source	MO: 95.08 %, k= 0.0343 min^{-1} TC: 93.28 %, k= 0.0200 min^{-1}	[34]

Pollutants: IMD-imidacloprid, PVA-Polyvinyl alcohol, RB-Rhodamine B, MO-methyl orange, MB-methylene blue, TC-tetracycline hydrochloride.

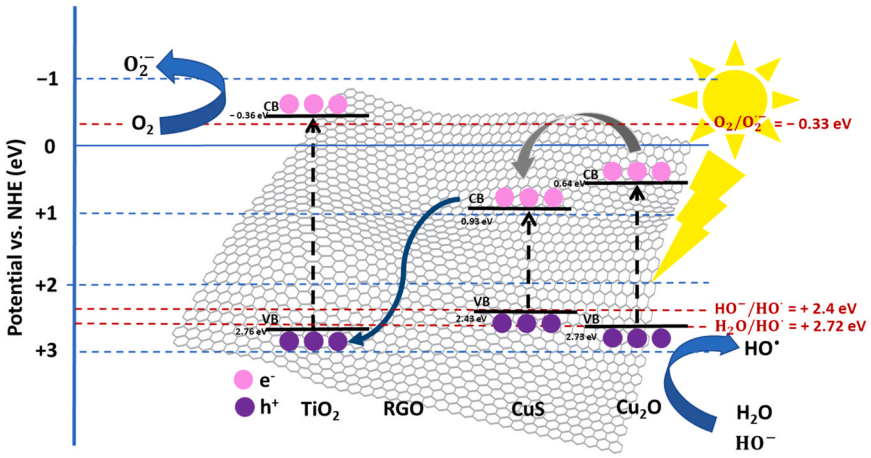

Fig. 9. Proposed mechanism of the TiO_2@Cu_2O-CuS heterostructure mediated by RGO for IMD photodegradation unde full-spectrum irradiation.

determination of the band gap energy E_g using UV-Vis DRS (Table 2), semiconductor electronegativity ($\chi_{Semiconductor}$), and E_e, the energy of free electrons relative to hydrogen (4.5 eV). The absolute semiconductor electronegativity ($\chi_{Semiconductor}$, eV) and the absolute cationic electronegativity (χ_{cation}, eV) are calculated using Eq. 9 and Eq. 10, where χ_{cation} (P.u.) represents the cationic electronegativity in Pauling units.

$$E_{VB} = \chi_{Seminconductor} - E_e + 0.5 \bullet E_g \tag{7}$$

$$E_{CB} = E_{VB} - E_g \tag{8}$$

$$\chi_{Semiconductor}(eV) = 0.45 \bullet \chi_{cation}(eV) + 3.36 \tag{9}$$

$$\chi_{cation}(eV) = \frac{\chi_{cation}(P.u.) + 0.206}{0.336} \tag{10}$$

The mechanism encompasses several steps as follows:

1. *Light absorption and excitation for generation of charge carriers*: When the TiO_2/RGO/Cu_2O-CuS heterostructure is exposed to full-spectrum irradiation, Cu_2O, with a band gap (E_g) of 2.09 eV, absorbs photons. This absorption results in the excitation of electrons (e^-) from the valence band (VB) (at 2.73 eV) to the conduction band (CB) (at 0.64 eV) of Cu_2O, by absorbing photons from the full UV–VIS–NIR spectrum, simultaneously creating holes (h^+) in the VB.
2. *Charge separation and transfer*: Due to the potential gradient provided by the heterojunction, e^- in the CB of Cu_2O (at 0.64 eV) can transfer to the CB of CuS (at 0.93 eV). This transfer is thermodynamically favorable as the CB of CuS is at a higher energy level than that of Cu_2O. Electrons can then be transferred from CuS to TiO_2 through the RGO layer due to its high electrical conductivity, acting as a bridge between the CB of CuS and the VB of TiO_2.
3. *Surface reactions and radical formation:* Electrons in the CB of TiO_2 (at −0.36 eV) react with molecular oxygen (O_2) to form superoxide radicals ($O_2^{\bullet-}$). The positive holes left in the VB of Cu_2O can react with hydroxide ions (HO^-) and water molecules (H_2O) to generate hydroxyl radicals ($HO^{\bullet}$), which are powerful oxidizing agents.
4. *Photocatalytic activity*: The hydroxyl and superoxide radicals generated can effectively degrade organic pollutants, such as imidacloprid (IMD), by breaking their chemical bonds through oxidation reactions.
5. *Suppression of electron-hole pairs* recombination: RGO minimizes the recombination rate of e^- and h^+, thus increasing the quantum yield of the photocatalytic reactions.
6. *System Regeneration:* After the reaction, the charge carriers may recombine, releasing energy as heat, or they may be scavenged by the photocatalyst itself, returning the system to its ground state, ready for another cycle of light absorption and pollutant degradation.

4. Summary and conclusion

This study has successfully developed and characterized a novel TiO_2/RGO/Cu_2O-CuS, heterostructure which exhibits remarkable photocatalytic efficiency in the degradation of imidacloprid, a common organic pollutant, under full-spectrum solar irradiation. This heterostructure leverages the complementary properties of its constituent materials—TiO_2, Cu_2O-CuS, and RGO—to enhance photocatalytic activity beyond what each material could achieve individually. The TiO_2/RGO/Cu_2O-CuS configuration shows over 95 % degradation efficiency of imidacloprid under simulated solar irradiation, attributed to the charge carrier dynamics facilitated by the strategic integration of RGO, which enhances charge transfer and reduces electron-hole recombination. The study highlights the importance of material layer sequencing in the heterostructure's assembly, showing that the sequence in which the materials are layered can significantly impact the photocatalytic efficiency. The TiO_2/RGO/Cu_2O-CuS configuration, in particular, facilitates efficient light absorption, charge separation, and transfer, leading to superior photocatalytic activity. The favorable energy band alignment between TiO_2 and Cu_2O-CuS, along with the charge mediation role of RGO, are critical factors that contribute to the system's effectiveness in imidacloprid degradation. The heterostructure demonstrates excellent stability and recyclability, maintaining high photocatalytic efficiency even after multiple degradation cycles. This durability, combined with the system's ability to efficiently utilize the full spectrum of solar irradiation, underscores its potential for sustainable pollutant removal applications.

CRediT authorship contribution statement

Luminita Andronic: Writing – review & editing, Writing – original draft, Validation, Resources, Project administration, Methodology, Investigation, Funding acquisition, Data curation, Conceptualization. **Coset Abreu Abreu-Jaureguí:** Writing – original draft, Visualization, Investigation, Formal analysis, Data curation. **Joaquin Silvestre-Albero:** Writing – review & editing, Supervision, Resources, Project administration, Methodology, Funding acquisition, Conceptualization.

Declaration of Competing Interest

The authors declare the following financial interests/personal relationships which may be considered as potential competing interests. Andronic Luminita reports financial support, administrative support,

equipment, drugs, or supplies, and writing assistance were provided by Executive Unit for Financing Higher Education Research Development and Innovation. Joaquin Silvestre Albero reports financial support, administrative support, equipment, drugs, or supplies, and writing assistance were provided by Agencia Estatal de Investigación, Spain. Coset Abreu Jauregui reports financial support, equipment, drugs, or supplies, statistical analysis, and writing assistance were provided by Agencia Estatal de Investigación, Spain. If there are other authors, they declare that they have no known competing financial interests or personal relationships that could have appeared to influence the work reported in this paper.

Data availability

No data was used for the research described in the article.

Acknowledgements

This work was supported by a grant from the Romanian National Authority for Scientific Research and Innovation, CCCDI-UEFISCDI, Project number 169/2020 ERANET-M.-3D-Photocat, within PNCDI III and MCIN/AEI/10.13039/501100011033 and EU NextGeneration/PRTR (Project PCI2020- 111968/3D-Photocat).

Appendix A. Supporting information

Supplementary data associated with this article can be found in the online version at doi:10.1016/j.jallcom.2024.174682.

References

[1] I.V. Yentekakis, F. Dong, Grand challenges for catalytic remediation in environmental and energy applications toward a cleaner and sustainable future, Front. Environ. Chem. 1 (2020), https://doi.org/10.3389/fenvc.2020.00005.
[2] L. Rizzo, S. Malato, D. Antakyali, V.G. Beretsou, M.B. Đolić, W. Gernjak, E. Heath, I. Ivancev-Tumbas, P. Karaolia, A.R. Lado Ribeiro, G. Mascolo, C.S. McArdell, H. Schaar, A.M.T. Silva, D. Fatta-Kassinos, Consolidated vs new advanced treatment methods for the removal of contaminants of emerging concern from urban wastewater, Sci. Total Environ. 655 (2019) 986–1008, https://doi.org/10.1016/j.scitotenv.2018.11.265.
[3] L.C. Ferreira, M. Castro-Alférez, S. Nahim-Granados, M.I. Polo-López, M.S. Lucas, G. Li Puma, P. Fernández-Ibáñez, Inactivation of water pathogens with solar photoactivated persulfate oxidation, Chem. Eng. J. 381 (2020) 122275, https://doi.org/10.1016/j.cej.2019.122275.
[4] M.M. Mahlambi, C.J. Ngila, B.B. Mamba, Recent developments in environmental photocatalytic degradation of organic pollutants: the case of titanium dioxide nanoparticles—a review, J. Nanomater. 2015 (2015) 1–29, https://doi.org/10.1155/2015/790173.
[5] W. Bahnemann, M. Muneer, M.M. Haque, Titanium dioxide-mediated photocatalysed degradation of few selected organic pollutants in aqueous suspensions, Catal. Today 124 (2007) 133–148, https://doi.org/10.1016/j.cattod.2007.03.031.
[6] S. Murgolo, S. Franz, H. Arab, M. Bestetti, E. Falletta, G. Mascolo, Degradation of emerging organic pollutants in wastewater effluents by electrochemical photocatalysis on nanostructured TiO_2 meshes, Water Res 164 (2019) 114920, https://doi.org/10.1016/j.watres.2019.114920.
[7] A.K. Priya, L. Gnanasekaran, S. Rajendran, J. Qin, Y. Vasseghian, Occurrences and removal of pharmaceutical and personal care products from aquatic systems using advanced treatment- a review, Environ. Res. 204 (2022) 112298, https://doi.org/10.1016/j.envres.2021.112298.
[8] C.O. Okoye, E.S. Okeke, K.C. Okoye, D. Echude, F.A. Andong, K.I. Chukwudozie, H. U. Okoye, C.D. Ezeonyejiaku, Occurrence and fate of pharmaceuticals, personal care products (PPCPs) and pesticides in African water systems: a need for timely intervention, Heliyon 8 (2022) e09143, https://doi.org/10.1016/j.heliyon.2022.e09143.
[9] N. Mumtaz, A. Javaid, M. Imran, S. Latif, N. Hussain, S. Nawaz, M. Bilal, Nanoengineered metal-organic framework for adsorptive and photocatalytic mitigation of pharmaceuticals and pesticide from wastewater, Environ. Pollut. 308 (2022) 119690, https://doi.org/10.1016/j.envpol.2022.119690.
[10] K. Babić, V. Tomašić, V. Gilja, J. Le Cunff, V. Gomzi, A. Pintar, G. Žerjav, S. Kurajica, M. Duplančić, I.E. Zelić, T.V. Pavičić, I. Grčić, Photocatalytic degradation of imidacloprid in the flat-plate photoreactor under UVA and simulated solar irradiance conditions—The influence of operating conditions, kinetics and degradation pathway, J. Environ. Chem. Eng. 9 (2021) 105611, https://doi.org/10.1016/j.jece.2021.105611.
[11] M. Xue, P. Li, C. Li, Y. Qi, Z. Han, J. Li, A. Li, T. Xia, Transformation of graphene oxide affects photodegradation of imidacloprid in the aquatic environment: mechanism and implication, Sci. Total Environ. 879 (2023) 163108, https://doi.org/10.1016/j.scitotenv.2023.163108.
[12] M. Malakootian, A. Shahesmaeili, M. Faraji, H. Amiri, S. Silva Martinez, Advanced oxidation processes for the removal of organophosphorus pesticides in aqueous matrices: a systematic review and meta-analysis, Process Saf. Environ. Prot. 134 (2020) 292–307, https://doi.org/10.1016/j.psep.2019.12.004.
[13] M. Radović Vučić, R. Baošić, J. Mitrović, M. Petrović, N. Velinov, M. Kostić, A. Bojić, Comparison of the advanced oxidation processes in the degradation of pharmaceuticals and pesticides in simulated urban wastewater: principal component analysis and energy requirements, Process Saf. Environ. Prot. 149 (2021) 786–793, https://doi.org/10.1016/j.psep.2021.03.039.
[14] C. Xia, X. Li, Y. Wu, S. Suharti, Y. Unpaprom, A. Pugazhendhi, A review on pollutants remediation competence of nanocomposites on contaminated water, Environ. Res. 222 (2023) 115318, https://doi.org/10.1016/j.envres.2023.115318.
[15] P. Alulema-Pullupaxi, P.J. Espinoza-Montero, C. Sigcha-Pallo, R. Vargas, L. Fernández, J.M. Peralta-Hernández, J.L. Paz, Fundamentals and applications of photoelectrocatalysis as an efficient process to remove pollutants from water: a review, Chemosphere 281 (2021) 130821, https://doi.org/10.1016/j.chemosphere.2021.130821.
[16] M. Pelaez, N.T. Nolan, S.C. Pillai, M.K. Seery, P. Falaras, A.G. Kontos, P.S. M. Dunlop, J.W.J. Hamilton, J.A. Byrne, K. O'Shea, M.H. Entezari, D.D. Dionysiou, A review on the visible light active titanium dioxide photocatalysts for environmental applications, Appl. Catal. B Environ. 125 (2012) 331–349, https://doi.org/10.1016/j.apcatb.2012.05.036.
[17] F.M. Sanakousar, C.C. Vidyasagar, V.M. Jiménez-Pérez, K. Prakash, Recent progress on visible-light-driven metal and non-metal doped ZnO nanostructures for photocatalytic degradation of organic pollutants, Mater. Sci. Semicond. Process. 140 (2022) 106390, https://doi.org/10.1016/j.mssp.2021.106390.
[18] W.S. Koe, J.W. Lee, W.C. Chong, Y.L. Pang, L.C. Sim, An overview of photocatalytic degradation: photocatalysts, mechanisms, and development of photocatalytic membrane, Environ. Sci. Pollut. Res. 27 (2020) 2522–2565, https://doi.org/10.1007/s11356-019-07193-5.
[19] U.I. Gaya, A.H. Abdullah, Heterogeneous photocatalytic degradation of organic contaminants over titanium dioxide: a review of fundamentals, progress and problems, J. Photochem. Photobiol. C. Photochem. Rev. 9 (2008) 1–12, https://doi.org/10.1016/j.jphotochemrev.2007.12.003.
[20] S. Kanan, M.A. Moyet, R.B. Arthur, H.H. Patterson, Recent advances on TiO 2 -based photocatalysts toward the degradation of pesticides and major organic pollutants from water bodies, Catal. Rev. 62 (2020) 1–65, https://doi.org/10.1080/01614940.2019.1613323.
[21] X. Kang, S. Liu, Z. Dai, Y. He, X. Song, Z. Tan, Titanium dioxide: from engineering to applications, Catalysts 9 (2019) 191, https://doi.org/10.3390/catal9020191.
[22] R. Zhang, L. Zhang, Q. Zheng, P. Gao, J. Zhao, J. Yang, Direct Z-Scheme Water Splitting Photocatalyst Based on Two-Dimensional Van Der Waals Heterostructures, J. Phys. Chem. Lett. 9 (2018) 5419–5424, https://doi.org/10.1021/acs.jpclett.8b02369.
[23] R. Acharya, K. Parida, A review on TiO_2/g-C_3N_4 visible-light- responsive photocatalysts for sustainable energy generation and environmental remediation, J. Environ. Chem. Eng. 8 (2020) 103896, https://doi.org/10.1016/j.jece.2020.103896.
[24] W.-K. Jo, N.C.S. Selvam, Z-scheme CdS/g-C_3N_4 composites with RGO as an electron mediator for efficient photocatalytic H_2 production and pollutant degradation, Chem. Eng. J. 317 (2017) 913–924, https://doi.org/10.1016/j.cej.2017.02.129.
[25] N.T.T. Truc, D.S. Duc, D. Van Thuan, T.Al Tahtamouni, T.-D. Pham, N.T. Hanh, D. T. Tran, M.V. Nguyen, N.M. Dang, N.T.P. Le Chi, V.N. Nguyen, The advanced photocatalytic degradation of atrazine by direct Z-scheme Cu doped ZnO/g-C_3N_4, Appl. Surf. Sci. 489 (2019) 875–882, https://doi.org/10.1016/j.apsusc.2019.05.360.
[26] P. Hemmatpour, A. Nezamzadeh-Ejhieh, A Z-scheme CdS/$BiVO_4$ photocatalysis towards Eriochrome black T: an experimental design and mechanism study, Chemosphere 307 (2022) 135925, https://doi.org/10.1016/j.chemosphere.2022.135925.
[27] S. Singla, S. Sharma, S. Basu, MoS_2/WO_3 heterojunction with the intensified photocatalytic performance for decomposition of organic pollutants under the broad array of solar light, J. Clean. Prod. 324 (2021) 129290, https://doi.org/10.1016/j.jclepro.2021.129290.
[28] J. Li, H. Yuan, Z. Zhu, Fabrication of Cu_2O/Au/$BiPO_4$ Z-scheme photocatalyst to improve the photocatalytic activity under solar light, J. Mol. Catal. A Chem. 410 (2015) 133–139, https://doi.org/10.1016/j.molcata.2015.09.013.
[29] X. Qi, T. Jin, Y. Liu, Y. Tian, Y. Liu, S. Chi, J. Zhang, Y. Hu, D. Fang, J. Wang, Construction of a dual Z-scheme Cu|Cu_2O/TiO_2/CuO photocatalyst composite film with magnetic field enhanced photocatalytic activity, Sep. Purif. Technol. 301 (2022) 122019, https://doi.org/10.1016/j.seppur.2022.122019.
[30] J. Ma, C. Liang, C. Yu, H. Li, H. Xu, Y. Hua, C. Wang, BiOBr microspheres anchored with Cu_2O nanoparticles and rGO: A Z-scheme heterojunction photocatalyst for efficient reduction of Cr(VI) under visible light irradiation, Appl. Surf. Sci. 609 (2023) 155247, https://doi.org/10.1016/j.apsusc.2022.155247.
[31] X. Yao, Y. Jawad BahrAluloom, S. Farhan Jawad, T. Hafdhi Abdtawfeeq, D. Rahman Al-janabi, N. Ahmad, A.M. Alshehri, S.K. Hadrawi, M. Mohammed Al-Taee, Y. Riadi, B. Jushi Janani, A. Fakhri, Multipurpose properties the Z-scheme dimanganese copper oxide/cadmium sulfide nanocomposites for photo- or photoelectro-catalytic, antibacterial applications, and thiamine detection process, J. Photochem. Photobiol. A Chem. 436 (2023) 114374, https://doi.org/10.1016/j.jphotochem.2022.114374.

[32] J. Zhang, J. Li, Q. Zhang, D. Guo, Constructing a novel CuS/Cu_2S Z-scheme heterojunction for highly-efficiency NIR light-driven antibacterial activity, Appl. Surf. Sci. 624 (2023) 156848, https://doi.org/10.1016/j.apsusc.2023.156848.
[33] R. Zhang, J. Yu, T. Zhang, C. Zhao, Q. Han, Y. Li, Y. Liu, K. Zeng, L. Cai, Z. Yang, Y. Ma, A novel snowflake dual Z-scheme Cu_2S/RGO/Bi_2WO_6 photocatalyst for the degradation of bisphenol A under visible light and its effect on crop growth, Colloids Surf. A Physicochem. Eng. Asp. 641 (2022) 128526, https://doi.org/10.1016/j.colsurfa.2022.128526.
[34] H. Xiong, K. Yin, L. Wang, J. Wang, Z. Hai, Obvious enhancement of visible photocatalytic performance of Cu_2O modified with TiO_2-g-C_3N_4: A strategy to achieve synergistic effect of p-n junction and Z-scheme, Opt. Mater. (Amst.). 138 (2023) 113727, https://doi.org/10.1016/j.optmat.2023.113727.
[35] J. Wu, B. Liu, Z. Ren, M. Ni, C. Li, Y. Gong, W. Qin, Y. Huang, C.Q. Sun, X. Liu, CuS/RGO hybrid photocatalyst for full solar spectrum photoreduction from UV/Vis to near-infrared light, J. Colloid Interface Sci. 517 (2018) 80–85, https://doi.org/10.1016/j.jcis.2017.09.042.
[36] J.-H. Lee, T. Kim, E.-R. Kim, E.-B. Cho, S.-C. Jung, Microwave-assisted synthesis of various Cu_2O/Cu/TiO_2 and Cu_xS/TiO_2 composite nanoparticles towards visible-light photocatalytic applications, Mater. Chem. Phys. 259 (2021) 123986, https://doi.org/10.1016/j.matchemphys.2020.123986.
[37] Q. Liu, J. Shen, X. Yang, T. Zhang, H. Tang, 3D reduced graphene oxide aerogel-mediated Z-scheme photocatalytic system for highly efficient solar-driven water oxidation and removal of antibiotics, Appl. Catal. B Environ. 232 (2018) 562–573, https://doi.org/10.1016/j.apcatb.2018.03.100.
[38] X. Chen, S. Shen, L. Guo, S.S. Mao, Semiconductor-based photocatalytic hydrogen generation, Chem. Rev. 110 (2010) 6503–6570, https://doi.org/10.1021/cr1001645.
[39] X. Xia, M. Song, H. Wang, X. Zhang, N. Sui, Q. Zhang, V.L. Colvin, W.W. Yu, Latest progress in constructing solid-state Z scheme photocatalysts for water splitting, Nanoscale 11 (2019) 11071–11082, https://doi.org/10.1039/C9NR03218E.
[40] T. Takayama, K. Sato, T. Fujimura, Y. Kojima, A. Iwase, A. Kudo, Photocatalytic CO_2 reduction using water as an electron donor by a powdered Z-scheme system consisting of metal sulfide and an RGO–TiO_2 composite, Faraday Discuss. 198 (2017) 397–407, https://doi.org/10.1039/C6FD00215C.
[41] X. Li, J. Yu, M. Jaroniec, X. Chen, Cocatalysts for selective photoreduction of CO_2 Into Solar Fuels, Chem. Rev. 119 (2019) 3962–4179, https://doi.org/10.1021/acs.chemrev.8b00400.
[42] X. Yang, L. Tian, X. Zhao, H. Tang, Q. Liu, G. Li, Interfacial optimization of g-C_3N_4-based Z-scheme heterojunction toward synergistic enhancement of solar-driven photocatalytic oxygen evolution, Appl. Catal. B Environ. 244 (2019) 240–249, https://doi.org/10.1016/j.apcatb.2018.11.056.
[43] W.S. Hummers, R.E. Offeman, Preparation of graphitic oxide, J. Am. Chem. Soc. 80 (1958) 1339, https://doi.org/10.1021/ja01539a017.
[44] V. Verma, L. Gurnani, A. Das, N. Kumari, T. Dasgupta, A. Mukhopadhyay, Reduced graphene oxides prepared via explosive and non-explosive thermal reduction: structural evolution, functional properties and reinforcing efficacy, Carbon N. Y. 209 (2023) 118007, https://doi.org/10.1016/j.carbon.2023.118007.
[45] S. Azizighannad, S. Mitra, Stepwise reduction of graphene oxide (GO) and its effects on chemical and colloidal properties, Sci. Rep. 8 (2018) 10083, https://doi.org/10.1038/s41598-018-28353-6.
[46] L.Y. Wong, S.Y. Lau, S. Pan, M.K. Lam, 3D graphene-based adsorbents: synthesis, proportional analysis and potential applications in oil elimination, Chemosphere 287 (2022) 132129, https://doi.org/10.1016/j.chemosphere.2021.132129.
[47] C.P.Pousa Soares, R. de Lacerda Baptista, D.V. Cesar, Solvothermal reduction of graphite oxide using alcohols, Mater. Res. 21 (1) (2018) 7, https://doi.org/10.1590/1980-5373-MR-2017-0726.
[48] L. Samet, K. March, O. Stephan, N. Brun, F. Hosni, F. Bessousa, J. Benasseur, R. Chtourou, Radiocatalytic Cu-incorporated TiO2 nano-particles for the degradation of organic species under gamma irradiation, J. Alloy. Compd. 743 (2018) 175–186, https://doi.org/10.1016/j.jallcom.2018.02.001.
[49] C.H. Zhou, S. Xu, Y. Yang, B.C. Yang, H. Hu, Z.C. Quan, B. Sebo, B.L. Chen, Q. D. Tai, Z.H. Sun, X.Z. Zhao, Titanium dioxide sols synthesized by hydrothermal methods using tetrabutyl titanate as starting material and the application in dye sensitized solar cells, Electrochim. Acta 56 (2011) 4308–4314, https://doi.org/10.1016/j.electacta.2011.01.054.
[50] K. Li, D. Zhao, Y. Li, S. Luo, Z. Zhou, The synergistic photocatalytic effects of surface-modified g-C_3N_4 in simple and complex pollution systems based on a macro-thermodynamic model, Environ. Sci. Nano. 8 (2021) 217–232, https://doi.org/10.1039/D0EN00759E.
[51] A.C. Fernandes, M.L. Pinto, F. Antunes, J. Pires, Synthetic cobalt clays for the storage and slow release of therapeutic nitric oxide, RSC Adv. 6 (2016) 41195–41203, https://doi.org/10.1039/C6RA05794B.
[52] T. Raguram, K.S. Rajni, E. Nandhakumar, G. Kiruthiga, Investigation on copper–nickel co-doped anatase titania nanospheres as an efficient material for photocatalytic and photovoltaic applications, N. J. Chem. (2023), https://doi.org/10.1039/D3NJ02697C.
[53] H. Huang, Y. Qiao, Y. Yuan, J. Zhang, in: Y. Yin, Y. Lu, Y.B.T.-E. of N. (First E. Xia) (Eds.), Surface Functionalization for Heterogeneous Catalysis, Elsevier, Oxford, 2023, pp. 407–419, https://doi.org/10.1016/B978-0-12-822425-0.00073-7.
[54] N. Zhang, M.-Q. Yang, S. Liu, Y. Sun, Y.-J. Xu, Waltzing with the versatile platform of graphene to synthesize composite photocatalysts, Chem. Rev. 115 (2015) 10307–10377, https://doi.org/10.1021/acs.chemrev.5b00267.
[55] Waris, A. Hakeem Anwer, F. Abdulaziz, S. Latif, A. Alanazi, S. Sultana, M. Zain Khan, Microwave assisted green synthesis of high capacitive TiO_2 doped rGO nanosheets for supercapacitor applications, Mater. Sci. Eng. B. 291 (2023) 116367, https://doi.org/10.1016/j.mseb.2023.116367.
[56] H. Liu, S. Yuan, J. Deng, Y. Zhao, X. Xie, J. Liu, Effects of loaded-mineral elements on CO enhancement of wheat straw pyrolysis in low-concentration CO_2 atmosphere, J. Anal. Appl. Pyrolysis 172 (2023) 106025, https://doi.org/10.1016/j.jaap.2023.106025.
[57] L. Andronic, L. Isac, A. Duta, Photochemical synthesis of copper sulphide/titanium oxide photocatalyst, J. Photochem. Photobiol. A Chem. 221 (2011) 30–37, https://doi.org/10.1016/j.jphotochem.2011.04.018.
[58] L. Isac, L. Andronic, A. Enesca, A. Duta, Copper sulfide films obtained by spray pyrolysis for dyes photodegradation under visible light irradiation, J. Photochem. Photobiol. A Chem. 252 (2013) 53–59, https://doi.org/10.1016/j.jphotochem.2012.11.011.
[59] T. Čižmar, I. Panžić, I. Capan, A. Gajović, Nanostructured TiO_2 photocatalyst modified with Cu for improved imidacloprid degradation, Appl. Surf. Sci. 569 (2021) 151026, https://doi.org/10.1016/j.apsusc.2021.151026.
[60] D. Mohanta, M. Ahmaruzzaman, Au–SnO_2–CdS ternary nanoheterojunction composite for enhanced visible light-induced photodegradation of imidacloprid, Environ. Res. 201 (2021) 111586, https://doi.org/10.1016/j.envres.2021.111586.
[61] H. Targhan, A. Rezaei, A. Aliabadi, H. Zheng, H. Cheng, T.M. Aminabhavi, Adsorptive and photocatalytic degradation of imidacloprid pesticide from wastewater via the fabrication of ZIF-CdS/Tpy quantum dots, Chem. Eng. J. 482 (2024) 148983, https://doi.org/10.1016/j.cej.2024.148983.
[62] A.L.T. Zheng, S. Sabidi, T. Ohno, T. Maeda, Y. Andou, Cu_2O/TiO_2 decorated on cellulose nanofiber/reduced graphene hydrogel for enhanced photocatalytic activity and its antibacterial applications, Chemosphere 286 (2022) 131731, https://doi.org/10.1016/j.chemosphere.2021.131731.
[63] R. Basumatary, D. Konwar, B. Basumatary, A. Ramchiary, Plasmonic enhanced branched Ag sensitized Cu_2O–CuO/TiO_2 heterojunction with unprecedented photocatalytic degradation under visible light, J. Phys. Chem. Solids 180 (2023) 111435, https://doi.org/10.1016/j.jpcs.2023.111435.
[64] M. Sun, Y. Fang, Y. Wang, S. Sun, J. He, Z. Yan, Synthesis of Cu_2O/graphene/rutile TiO_2 nanorod ternary composites with enhanced photocatalytic activity, J. Alloy. Compd. 650 (2015) 520–527, https://doi.org/10.1016/j.jallcom.2015.08.002.
[65] L. Yang, X. Guan, G.-S. Wang, X.-H. Guan, B. Jia, Synthesis of ZnS/CuS nanospheres loaded on reduced graphene oxide as high-performance photocatalysts under simulated sunlight irradiation, New J. Chem. 41 (2017) 5732–5744, https://doi.org/10.1039/C7NJ00801E.